

The SAURON project - VII. Integral-field absorption and emission-line kinematics of 24 spiral galaxy bulges

Jesús Falcón-Barroso^{1*}, Roland Bacon², Martin Bureau³, Michele Cappellari¹, Roger L. Davies³, P.T. de Zeeuw¹, Eric Emsellem², Kambiz Fathi⁴, Davor Krajnović³, Harald Kuntschner⁵, Richard M. McDermid¹, Reynier F. Peletier^{6,7}, Marc Sarzi³

¹*Sterrewacht Leiden, Niels Bohrweg 2, 2333 CA Leiden, The Netherlands*

²*Centre de Recherche Astrophysique de Lyon - Observatoire, 9 Avenue Charles André, 69561 Saint Genis Laval, France*

³*Sub-Department of Astrophysics, University of Oxford, Denys Wilkinson Building, Keble Road, Oxford OX1 3RH, United Kingdom*

⁴*Rochester Institute of Technology, 84 Lomb Memorial Dr., Rochester, NY 14623-5603, USA*

⁵*Space Telescope European Coordinating Facility, European Southern Observatory, Karl-Schwarzschild-Str 2, 85748 Garching, Germany*

⁶*Kapteyn Astronomical Institute, P.O. Box 800, 9700 AV Groningen, The Netherlands*

⁷*School of Physics & Astronomy, University of Nottingham, Nottingham, NG7 2RD, United Kingdom*

29 November 2007

ABSTRACT

We present observations of the stellar and gas kinematics for a representative sample of 24 Sa galaxies obtained with our custom-built integral-field spectrograph SAURON operating on the William Herschel Telescope. The data have been homogeneously reduced and analysed by means of a dedicated pipeline. All resulting datacubes were spatially binned to a minimum mean signal-to-noise ratio of 60 per spatial and spectral resolution element. Our maps typically cover the bulge dominated region. We find a significant fraction of kinematically decoupled components (12/24), many of them displaying central velocity dispersion minima. They are mostly aligned and co-rotating with the main body of the galaxies, and are usually associated with dust discs and rings detected in unsharp-masked images. Almost all the galaxies in the sample (22/24) contain significant amounts of ionised gas which, in general, is accompanied by the presence of dust. The kinematics of the ionised gas is consistent with circular rotation in a disc co-rotating with respect to the stars. The distribution of mean misalignments between the stellar and gaseous angular momenta in the sample suggest that the gas has an internal origin. The [O III]/H β ratio is usually very low, indicative of current star formation, and shows various morphologies (ring-like structures, alignments with dust lanes or amorphous shapes). The star formation rates in the sample are comparable with that of normal disc galaxies. Low gas velocity dispersion values appear to be linked to regions of intense star formation activity. We interpret this result as stars being formed from dynamically cold gas in those regions. In the case of NGC 5953, the data suggest that we are witnessing the formation of a kinematically decoupled component from cold gas being acquired during the ongoing interaction with NGC 5954.

Key words: galaxies: bulges – galaxies: spiral – galaxies: kinematics and dynamics – galaxies: evolution – galaxies: formation – galaxies: ISM

1 INTRODUCTION

We are carrying out a study of the two-dimensional kinematic and stellar population properties of a representative sample of 72 early-type galaxies, primarily using integral-field observations obtained with SAURON (Bacon et al. 2001, hereafter Paper I). The main goals of the project are to study the intrinsic shapes, velocity and metallicity distributions of the sample galaxies, and to gain insight

into the relation between their stellar/gaseous kinematics and stellar populations. Details of the definition and properties of the survey can be found in de Zeeuw et al. (2002, hereafter Paper II). Previous papers of the series concentrated on the presentation and characterization of the stellar and ionised-gas kinematics and absorption line-strength indices of the sample of 48 elliptical and lenticular galaxies (Emsellem et al. 2004; Sarzi et al. 2005; Kuntschner et al. 2006, hereafter Papers III, V and VI). Here, we present the combined analysis of the stellar and ionised-gas distribution and kinematics of the 24 Sa galaxies in the representative sample. In addition, we investigate the importance of ongoing star formation in the

* jfalcon@strw.leidenuniv.nl

sample, and its relation to the dynamical state of the galaxies. For a more comprehensive study of an individual case in our sample (i.e., NGC 5448) we refer the reader to Fathi et al. (2005). Ganda et al. (2005) discuss similar SAURON observations of later-type spiral galaxies. The data and maps presented here will be made available via the SAURON website (<http://www.strw.leidenuniv.nl/sauron>).

The paper is structured as follows. Section 2 summarises the observations, instrumental setup and data reduction. Section 3 describes the tools employed to extract the stellar and ionised-gas kinematics. Section 4 shows the comparison of our results with aperture measurements in the literature. Section 5 is devoted to the presentation of the stellar and ionised-gas maps for each galaxy, as well as the description of the main features. Global and circumnuclear star formation is discussed in Section 6, and the results are summarised in Section 7. A more detailed description of the structures in the individual galaxies is presented in Appendix A.

2 OBSERVATIONS AND DATA REDUCTION

2.1 Observing runs and instrumental setup

Observations of the 24 Sa galaxies were carried out using the integral-field spectrograph SAURON attached to the 4.2-m William Herschel Telescope (WHT) of the Observatorio del Roque de los Muchachos at La Palma, Spain. For each of the 24 galaxies, Table 1 lists the run in which it was observed and the exposure time for each individual pointing. More details on the observing conditions in each run can be found in Paper III.

We used the low spatial resolution mode of SAURON, providing a $33'' \times 41''$ field-of-view (FoV). The spatial sampling is determined by an array of $0''.94 \times 0''.94$ square lenses. This setup produces 1431 spectra per pointing over the SAURON FoV. Additionally, 146 lenses provide simultaneous sky spectra $1''.9$ away from the main field. SAURON delivers a spectral resolution of 4.2 \AA (FWHM) and covers the narrow spectral range 4800–5380 \AA . This wavelength range includes a number of important stellar absorption lines (e.g. $H\beta$, Fe5015, Mg β , Fe5270) and also potential emission lines ($H\beta\lambda 4861$, $[O III]\lambda\lambda 4959, 5007$, $[N I]\lambda\lambda 5198, 5200$).

For each galaxy, four overlapping exposures of 1800 s were typically obtained. An offset of a few arcseconds, corresponding to a small, non-integer number of spatial elements, was introduced between exposures to avoid systematic errors due to e.g. bad CCD regions. While for most of the galaxies a single pointing was sufficient to cover the bulge dominated region, in three cases (NGC 2273, NGC 2844, NGC 3623) two pointings were required. Footprints of these pointings are shown overlaid on R -band Digital Sky Survey images in Figure 1.

2.2 Data reduction

We followed the procedures described in Paper I and III for the extraction, reduction, and calibration of the data, using the specifically designed XSAURON software developed at CRAL. For each galaxy, the sky level was measured using the dedicated sky lenses and subtracted from the target spectra. Arc lamp exposures were taken before and after each target frame for wavelength calibration. Tungsten lamp exposures were also taken at the beginning and end of each night in order to build the mask necessary to extract the data from the CCD frames. Flux and Lick absorption line standard stars were observed during each observing run for calibration purposes. Since the flux standards and the galaxies were not always observed

Table 1. Details of the exposures of the SAURON Sa spiral bulges.

Sa galaxies: Field				Sa galaxies: Cluster			
NGC (1)	Run (2)	# (3)	T_{exp} (4)	NGC (1)	Run (2)	# (3)	T_{exp} (4)
1056	6	1	4x1800	3623	3	1	4x1800
2273	5	1	4x1800		3	2	4x1800
	5	2	4x1800	4235	7	1	4x1800
2844	6	1	4x1800	4245	7	1	4x1800
	6	2	2x1800	4274	7	1	4x1800
4220	8	1	3x1800	4293	8	1	3x1800
4369	7	1	4x1800	4314	7	1	4x1800
5448	7	1	4x1800	4383	7	1	4x1800
5475	7	1	6x1800	4405	7	1	4x1800
5636	7	1	5x1800	4425	7	1	4x1800
5689	5	1	5x1800	4596	7	1	4x1800
5953	5	1	4x1800	4698	7	1	4x1800
6501	3	1	4x1800	4772	3	1	4x1800
7742	2	1	4x1800				

Notes: (1) NGC number. (2) Run number (see Table 1 in Paper III). (3) Pointing number. (4) Exposure time, in sec.

under the same conditions, the fluxes quoted in this paper are approximate. Differences in the flux calibration between observing runs are, however, smaller than 6% (see Paper VI). The individually extracted and flux calibrated datacubes were finally merged by truncating the wavelength domain to a common range and spatially resampling the spectra to a common squared grid. The dithering of individual exposures enabled us to sample the merged datacube onto $0''.8 \times 0''.8$ pixels.

During the eighth observing run, the grating of the instrument was replaced by a Volume Phase Holographic grating (VPH). This change gave an increase in sensitivity of the instrument. Only two galaxies in our sample are affected by this change (NGC 4220, NGC 4293). A specifically designed mask model (see Paper I for details) was produced for the extraction of the data in this run. All the procedures described above are valid for both configurations.

In order to ensure the measurement of reliable stellar kinematics, we spatially binned our final datacubes using the Voronoi 2D binning algorithm of Cappellari & Copin (2003), creating compact bins with a minimum signal-to-noise ratio (S/N) of ~ 60 per spectral resolution element. Most spectra in the central regions, however, have S/N in excess of 60, and so remain un-binned.

2.3 HST and ground-based imaging

In addition to the SAURON data, we retrieved from the *Hubble Space Telescope* (*HST*) archive¹ the available WFPC2 imaging closest to the F555W filter. The origin of the images is rather heterogeneous, so the final set of images used in this paper comes from observations made in several photometric filters. Since no *HST*/WFPC2 image was available for NGC 4220, ACS/F814W imaging was used instead. In the cases with no *HST* or with poor signal-to-noise imaging (e.g., *HST*/WFPC2/F300W) we used ground-based photometry, in the F555W and F814W filters, from the 1.3m McGraw-Hill telescope at the MDM observatory on Kitt

¹ Based on observations made with the NASA/ESA Hubble Space Telescope, obtained from the ESO/ST-ECF Science Archive Facility.

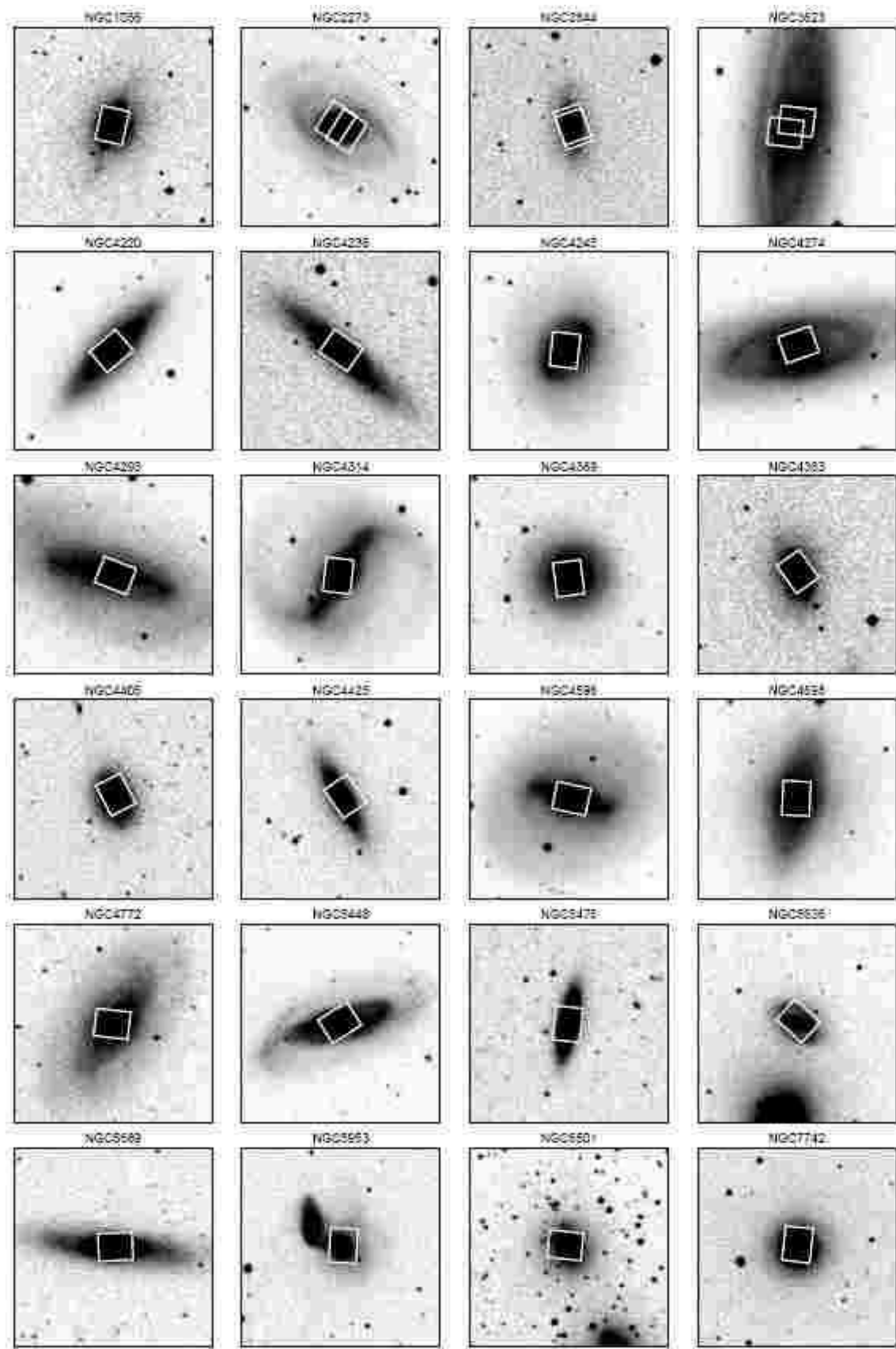


Figure 1. *R*-band Digital Sky Survey images of the 24 Sa spiral galaxy bulges in the SAURON representative sample. The size of each image is $4' \times 4'$, and the orientation is such that north is up and east is left. Overlaid on each image is the approximate field-of-view of the SAURON pointings obtained for the object.

Table 2. Characteristics of the SAURON Sa galaxies.

NGC	Type	V_{syst}	Source	Seeing	θ_s	$\Delta\phi_{\text{phot}}$	$\Delta\phi_{\text{kin}}$	$\log F_{\text{H}\beta}$	A_{gal}	A_{int}	$\log L_{\text{H}\alpha}$	$\log \text{SFR}$	$\log M_{\text{H II}}$
(1)	(2)	[km s^{-1}]	(4)	[arcsec]	[deg]	[deg]	[deg]	[$\text{erg s}^{-1} \text{cm}^{-2}$]	[mag]	[mag]	[erg s^{-1}]	[$M_{\odot} \text{yr}^{-1}$]	[M_{\odot}]
1056	Sa:	1564	WHT	2.0	96	4	6	-12.92	0.493	0.167	40.51	-0.59	5.88
2273	SBa(r):	1852	F606W	1.7	206	4	12	-13.09	0.235	0.122	40.37	-0.73	5.74
2844	Sa(r):	1510	WHT	1.5	243	1	5	-13.25	0.062	0.213	40.01	-1.10	5.37
3623	SAB(rs)	841	F814W	1.4	0	8	14	-13.13	0.083	0.357	39.68	-1.42	5.05
4220	S0 ⁺ (r)	946	F814W	2.3	313	15	9	-13.34	0.059	-	39.42	-1.68	4.79
4235	Sa(s)sp	2295	F606W	1.2	208	2	5	-13.63	0.062	0.357	40.05	-1.05	5.42
4245	SB0/a(r)	904	F606W	1.5	90	18	4	-13.39	0.069	0.053	39.36	-1.75	4.73
4274	(R)SBab(r)	930	F555W	1.7	154	5	21	-13.22	0.074	0.319	39.66	-1.45	5.03
4293	(R)SB0/a(s)	948	F606W	2.8	195	30	38	-13.61	0.130	0.122	39.23	-1.87	4.60
4314	SBa(rs)	1001	F814W	1.6	90	24	5	-12.83	0.083	0.015	40.00	-1.10	5.37
4369	(R)Sa(rs)	1043	WHT	1.4	76	29	12	-12.41	0.085	0.015	40.45	-0.65	5.82
4383	Sa pec	1724	F606W	0.9	228	1	5	-12.22	0.078	0.198	41.15	0.04	6.51
4405	S0/a(rs)	1750	F606W	1.8	236	5	2	-13.14	0.080	0.068	40.19	-0.91	5.56
4425	SB0 ⁺ :sp	1919	WHT	1.1	229	3	-	-	-	-	-	-	-
4596	SB0 ⁺ (r)	1910	F606W	2.2	6	16	8	-13.72	0.074	-	39.66	-1.44	5.03
4698	Sab(s)	1035	F606W	1.1	86	3	7	-13.17	0.086	0.213	39.51	-1.59	4.88
4772	Sa(s)	1068	F606W	1.6	0	34	30	-13.89	0.090	0.175	39.06	-2.05	4.43
5448	(R)SABa(r)	2043	F606W	1.1	141	13	1	-13.48	0.049	0.190	40.03	-1.08	5.39
5475	Sa sp	1667	F814W	1.3	90	2	57	-13.95	0.039	0.289	39.40	-1.70	4.77
5636	SAB(r)0+	1665	WHT	1.5	216	15	10	-13.90	0.109	-	39.37	-1.73	4.74
5689	SB0 ⁰ (s)	2225	F814W	1.9	171	2	9	-14.01	0.118	0.160	39.58	-1.52	4.95
5953	Sa:pec	2010	F606W	1.5	87	13	4	-12.60	0.162	0.076	40.88	-0.22	6.25
6501	S0 ⁺	2967	WHT	2.5	0	6	-	-	-	-	-	-	-
7742	Sb(r)	1678	F555W	1.6	270	30	1	-12.50	0.182	0.023	40.82	-0.28	6.19

Notes: (1) NGC number. (2) Hubble type from NED (<http://nedwww.ipac.caltech.edu/>). (3) Estimate of the heliocentric systemic velocity, in km s^{-1} , corrected for the barycentric motion. (4) Source for the seeing determination (see Sect. 2.3). (5) Seeing, full width at half maximum in arcsec. (6) Position angle, in degrees, of the vertical (upward) axis in the maps shown in Figs. 6a-6x. (7) Misalignment between the photometric and stellar kinematical major axis in degrees ($\Delta\phi_{\text{phot}} = |\phi_{\text{phot}} - \phi_{\text{star}}|$). (8) Misalignment between the major axis of the stellar and ionised-gas kinematics ($\Delta\phi_{\text{kin}} = |\phi_{\text{star}} - \phi_{\text{gas}}|$). The mean uncertainty in the measured misalignments in columns 7 and 8 is 6 and 7 degrees, respectively (see Section 5.3). (9) Observed $\text{H}\beta$ flux in the SAURON FoV. (10) V -band galactic extinction from Schlegel et al. (1998) as listed in NED. (11) V -band dust extinction due to inclination from Bottinelli et al. (1995). The original values in B -band, listed in Hyperleda, were converted to V -band assuming the attenuation law of Cardelli et al. (1989). (12) Estimated extinction corrected $\text{H}\alpha$ luminosity. (13) Total star formation rate within the SAURON FoV. (14) Mass of the ionised gas within the SAURON FoV. (See Section 6 for details).

Peak. The MDM images are part of a complete photometric survey of the SAURON galaxies and will be described elsewhere.

The use of this photometric dataset is two-fold. First, it allows us to generate unsharp-masked images, to highlight any small scale structures that might be present in the galaxies. Second, we used the HST images to accurately determine the point spread function (PSF) of each merged exposure, by comparing them to the reconstructed SAURON intensity distribution. We followed the procedure outlined in Paper III to derive the PSF values. Where HST imaging is not available, we quote the value from the seeing monitor during the observations. Table 2 summarises the HST imaging used (i.e., in the available filter closest to the V -band), and lists the seeing estimate for each galaxy. Cases with no HST imaging are indicated by WHT.

3 ANALYSIS AND METHODS

3.1 Stellar kinematics

We measured the stellar kinematics of the 24 Sa spiral bulges using the penalized pixel-fitting (pPXF) method of Cappellari & Emsellem (2004). We made use of the library of single age, single metallicity population (SSP) models from Vazdekis (1999) as stellar templates. We selected a representative

set of 48 SSP models evenly sampling a wide range in age and metallicity ($1.00 \leq \text{Age} \leq 17.38$ Gyr, $-1.68 \leq [\text{Fe}/\text{H}] \leq +0.20$). This set of templates differs from the one used in Paper III in that we expanded the range of metallicities to include more metal-poor templates. This was necessary to be able to accurately match the main absorption features in our galaxies. Exclusion of these models resulted in a poor match of the overall spectrum and therefore a bias in the measured parameters.

A non-negative linear combination of SSP models, convolved with a Gauss-Hermite series (van der Marel & Franx 1993; Gerhard 1993), was fitted to each individual spectrum. The best-fitting parameters were determined by chi-squared minimization in pixel space. In the wavelength range covered by SAURON, a few potential emission lines were masked during the fitting procedure ($\text{H}\beta$, $[\text{O III}]$, $[\text{N I}]$). Additionally, a low-order Legendre polynomial was included in the fit to account for small differences in the continuum shape between the galaxy spectra and the input library of synthetic models.

Our sample of spiral galaxies displays stellar velocity dispersions that are, in general, much lower than those found in the ellipticals and lenticulars in Paper III. Given the instrumental sampling of SAURON (60 km s^{-1} per pixel), some bias in the determination of the stellar velocity dispersion might be expected for values below $\sim 120 \text{ km s}^{-1}$. This bias can be minimised by choosing an ade-

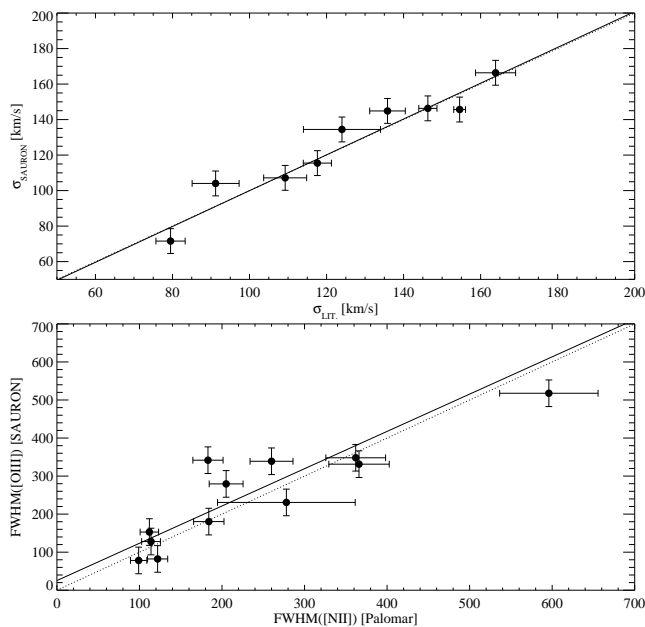


Figure 2. Comparison of kinematic parameters with the literature. Top: Central aperture measurements of the stellar velocity dispersion of the SAURON Sa spiral galaxies and values taken from Hyperleda. Bottom: Central aperture measurements of the [O III] ionised-gas FWHM of the SAURON Sa spiral galaxies and [N II] values taken from the Palomar spectroscopic survey (Ho et al. 1995, 1997a). Solid line represents a least-squares fit to the data points. The dotted line marks the 1:1 relation.

quate penalisation factor (λ) in pPXF. We carried out simulations to determine the best factor for our dataset, and a value of $\lambda = 0.7$ was adopted, as in Paper III. The level of uncertainty of the velocity dispersion σ , for this penalisation factor, was extensively tested in Paper III by means of Monte-Carlo simulations. As shown in Figure 2 of that paper, for a spectrum with a S/N of ~ 60 and an intrinsic σ as low as 50 km s^{-1} , the measured velocity dispersion differs from the intrinsic one by, at most, $\sim 10 \text{ km s}^{-1}$ even for extreme h_3 and h_4 values, which is within the estimated errors. In practice only the outer bins in our maps (i.e. the ones with the lowest velocity dispersions) are affected by this bias.

3.2 Gas kinematics

Typical spectra from our sample of galaxies contain significant amounts of nebular emission in the SAURON wavelength range. However, stellar absorption features are still dominant overall, and therefore the measurement of the gas distribution and kinematics requires a careful separation of the line emission from the stellar absorption. For this, we follow the procedure described in Paper V. Briefly, this method consists of searching iteratively for the emission-line velocities and velocity dispersions, while linearly solving at each step for both their amplitudes and the optimal combination of the stellar templates over the full SAURON wavelength range. No masking of the regions affected by emission is thus required. The stellar kinematics is held fixed during the fitting process. A low-order Legendre polynomial (typically of order 6) is included in the fit to account for small differences between the galaxy spectra and the input library of synthetic models. We refer the reader to Paper V for a more detailed description of the method, limitations, and sensitivity limits.

In general, the amount of emission in both $H\beta$ and [O III] is important in our sample. In some galaxies we are also able to detect significant emission from the [N I] doublet, but in most cases this is very weak and it is difficult to establish its kinematics. As observations of the $H\alpha$ and [N II] lines (e.g., Sofue et al. 1998), and the [N I] and [N II] emission lines (e.g., Goudfrooij & Emsellem 1996) display similar kinematics, we do not expect to find significant differences between the kinematics of $H\beta$ and [N I]. Given the small amount of information the [N I] maps add to our results, we do not show them here. They will be made available with the public data release.

As the ionised gas is collisional and dissipative, the emission-line maps can exhibit complicated morphologies and kinematics (Plana et al. 1998; Asif et al. 2005; Chemin et al. 2005, 2006). In practice this could translate into complex emission-line profiles due to the superposition of distinct gas clouds. We carefully inspected the emission line profiles in our data to search for asymmetric profiles, but we could not find any significant deviation from a pure Gaussian in the majority of our galaxies. Only a few cases revealed complex profiles in specific regions close to their centre, possibly related to their AGN nature (e.g., NGC 2273). The lack of such complex profiles in the rest of our sample may be, at least in part, due to SAURON’s limited spectral resolution. We therefore fitted a single Gaussian profile to each line in our wavelength range. We fixed the amplitude ratio of the [O III] emission-line doublet to 1:3 (Osterbrock 1989), and to 0.7:2 for the [N I] lines¹. As gas clouds may be ionised by different mechanisms, it is possible that in certain regions of the galaxies the ionisation of $H\beta$ is more efficient than [O III] and viceversa. Given that in general our sample galaxies display very strong emission, we looked for differences in the kinematics by fitting these two emission lines independently. Based on the simulations performed in Paper V, we considered true detection of emission when the ratio of the amplitude of the emission line to the surrounding noise (A/N , see Paper V) is larger than 5, 4, and 4 for $H\beta$, [O III], and [N I] respectively.

4 COMPARISON WITH THE LITERATURE

As demonstrated in Papers II, III and V for E and S0 galaxies, the methods used to derive the stellar and ionised-gas kinematics produce comparable results with those published in the literature. Here, we report similar comparisons to assess the robustness of these methods for our sample of Sa bulges, where emission is much more prominent and stellar velocity dispersions are smaller.

Literature measurements for our sample of Sa bulges are relatively scarce and come from heterogeneous sources, which often also implies different aperture sizes and slit position angles. We used the compilation in the on-line catalogue Hyperleda² (Prugniel & Simien 1996) for the comparison of the stellar kinematics, and the Palomar spectroscopic survey (Ho et al. 1995, 1997a) for the line-width of the ionised gas. We measured the stellar velocity dispersions and FWHM of the [O III] emission lines from a standard central aperture of $2'' \times 4''$ extracted from our SAURON maps. This aperture size was chosen to match the apertures in the Palomar survey. For the stellar velocity dispersions, apertures were aligned along the axis reported in the individual references (i.e.

¹ Ratio estimated using the Mappings Ic software with an electron temperature of 10^4 K and electron densities from 0.1 cm^{-3} to 1000 cm^{-3} (Ferruit et al. 1997)

² <http://leda.univ-lyon1.fr/>

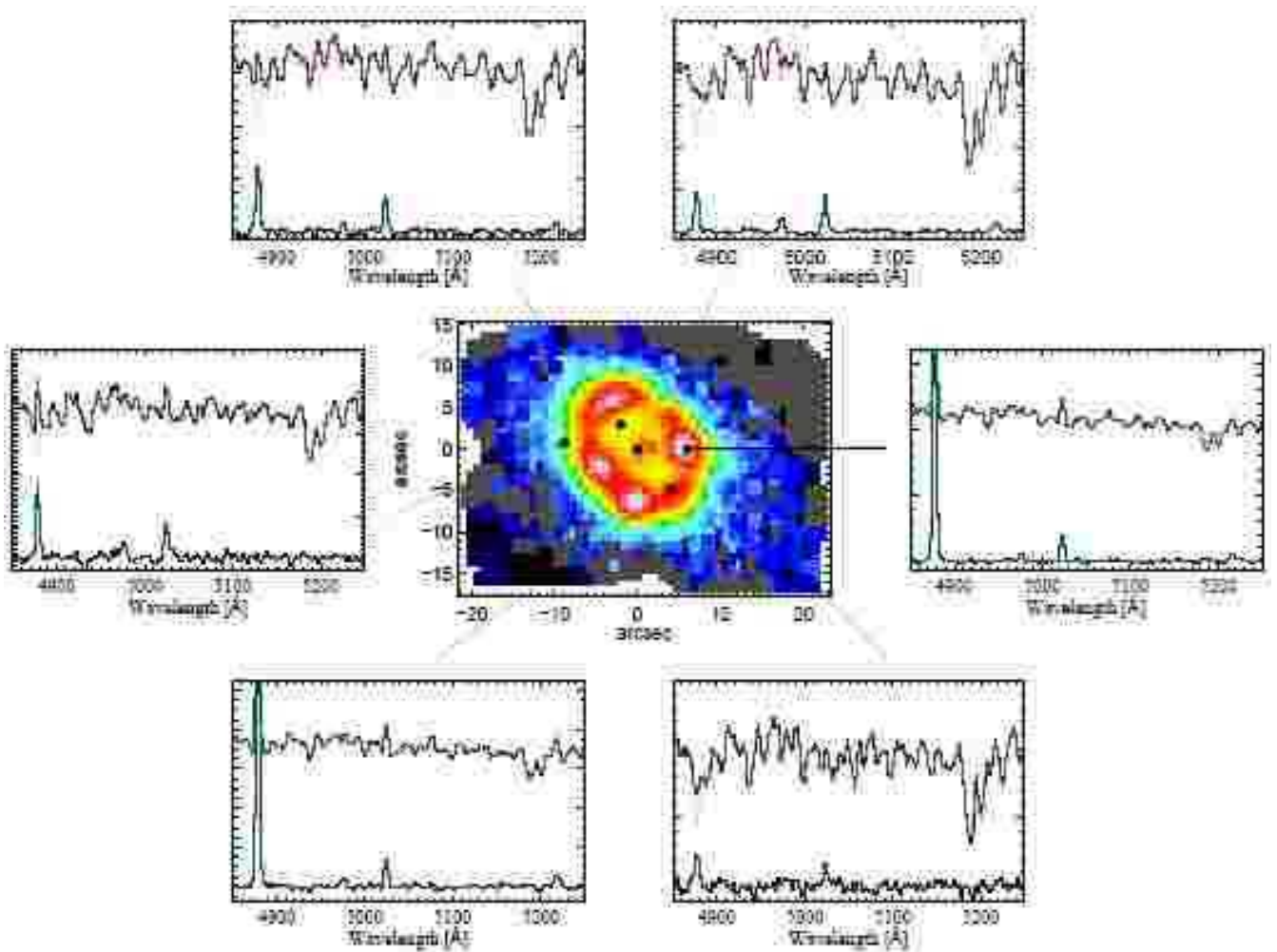


Figure 3. Fits of the SAURON spectra of NGC 4314. The inset corresponds to the $H\beta$ flux map (see also Fig. 6j). Data bins with A/N values below 5 (see 3.2) are displayed in the different maps as dark grey. Six spectra and their corresponding fits at different locations are shown around the inset image. In each panel the black line shows the galaxy spectrum, the red line is the best fitting stellar template, and the blue line is the best fit when emission lines are added. Below each spectrum the differences between the galaxy spectrum and the best stellar template are shown in black. The emission-line fits are overplotted in green. The spectra have been arbitrarily shifted in the vertical direction for presentation purposes.

Terlevich et al. 1990; di Nella et al. 1995; Rampazzo et al. 1995; Bernardi et al. 2002; Falc3n-Barroso et al. 2003). We only considered literature values with reported errors below 10 km s^{-1} (i.e., the typical error estimate of our measurements). For the ionised-gas measurements, we used the position angle of the Palomar long-slit observations. We excluded from the comparison galaxies with strong non-Gaussian emission-line profiles (i.e., AGN-like), as the single Gaussian used in our method is not an accurate representation of those line profiles. Uncertainties in the $[\text{N II}]$ FWHM in the Palomar survey were typically 10%, except in NGC 4596 for which the reported uncertainty is 40%.

On the top panel of Figure 2 we show the result of the comparison for the stellar velocity dispersions. A linear regression was fitted to the combined datasets. We made use of the *FITEXY*³ routine taken from the IDL Astro-Library (Landsman 1993) to fit a linear relation of the form $y = \alpha + \beta(x - x_0)$, where $y = \sigma_{\text{SAURON}}$ and $x = \sigma_{\text{LIT.}}$. The value of x_0 was chosen to be 150 km s^{-1}

to minimise the uncertainty in the fitted intercept. The resultant fit provides a slope of 1.01 ± 0.10 and an intercept of $150.40 \pm 3.53 \text{ km s}^{-1}$. Our measurements are thus in good agreement with those in the literature. On the bottom panel we plot the results for the ionised-gas FWHMs. A similar linear regression fit gives a slope of 0.98 ± 0.14 and intercept of $172.43 \pm 13.36 \text{ km s}^{-1}$. While a correlation between the $[\text{O III}]$ FWHM and $[\text{N II}]$ FWHM may be expected if these lines are produced in low-density reservoirs (Ho et al. 1997b), given the strong dependence of the line widths on the critical densities it is possible that this assumption does not hold for all galaxies in our sample. Considering this result and all the possible systematic effects at play in this comparison, our measurements seem to be in good agreement with those of Ho et al. (1997a).

Additionally, we tested the reliability of our measurements by checking the quality of the optimal template fits to the spectra in our galaxies. In Figure 3 we show these fits for one of the most critical cases in our sample: NGC 4314 (Benedict et al. 1992). We chose to illustrate this example because of the wide range of emission-line fluxes in the $H\beta$ map relative to the underlying stellar continuum. In

³ Based on a similar routine by Press et al. (1992)

this galaxy, most of the $H\beta$ emission is confined to a ring of radius $\sim 10''$. Outside the ring the amount of $H\beta$ flux decreases by more than a factor 100. The different panels in this figure demonstrate that our method is able to produce very good fits to the spectra in several distinct regions of the galaxy, and that our results are not biased because of an inadequate matching of the spectra. Similar agreement is found for the rest of the sample of galaxies.

5 OBSERVED STELLAR & GAS KINEMATICS

Figures 6a-6x display maps of the absorption and emission-line distribution and kinematics of the 24 Sa galaxies in our sample. The maps are displayed according to increasing NGC number. In each case, we show (*first row*) an unsharp-masked image of the galaxy from either HST or ground-based MDM data (see Section 2.3). The *second row* displays the total intensity reconstructed from the SAURON spectra (in mag/arcsec² with an arbitrary zero point), the mean stellar radial velocity V , and velocity dispersion σ (both in km s⁻¹). The *third and fourth row* presents the flux (in logarithmic scale), mean velocity and velocity dispersion (both in km s⁻¹) of the $H\beta$ and [O III] emission lines, respectively. The *fifth row* shows the [O III]/ $H\beta$ ratio map (in logarithmic scale), as well as the stellar Gauss-Hermite velocity moments h_3 and h_4 . The maps of the ionised gas were constructed according to the A/N ratios set in §3.2. Data bins with A/N values below these thresholds are displayed in dark grey. Mean stellar radial velocities are with respect to estimated heliocentric systemic velocities, the values of which are provided (corrected for the barycentric motion) in Table 2. The same heliocentric systemic velocity is assumed in the emission-line velocity maps.

Detailed descriptions of the different maps are collected in Appendix A. Here, we concentrate on an overview of the general trends and results observed.

5.1 Stellar kinematics

Inspection of the different figures reveals a wide range of kinematic structures. The presence of dust in our galaxies can have, in many cases, a strong impact on the measured stellar kinematics, as it affects the amount of light we receive along the line-of-sight. Despite the dust, and as expected for Sa galaxies, the maps show clear stellar rotation even at low galaxy inclinations (e.g., NGC 7742). Kinematically decoupled components occur frequently in the inner regions (NGC 1056, NGC 2273, NGC 3623, NGC 4235, NGC 4245, NGC 4274, NGC 4596, NGC 5448, NGC 5689, NGC 7742). These structures are usually detected in the stellar velocity maps alone (as a sudden change in velocity, or pinching of the isovelocity contours close to the centre), but often they are also associated with a drop in the velocity dispersion and anti-correlated h_3 values with respect to the stellar velocities. Moreover, they are generally related to features in the photometry, such as bars or central dust discs and rings. These structures are in nearly all cases co-rotating and aligned with the main body of the galaxy. The flattening of the isovelocities of these components suggests that these might be inner discs or rings. In addition, there are a few galaxies in the sample (NGC 4698 and NGC 5953) that have kinematically decoupled components which are misaligned with respect to the major axis of the galaxy.

Velocity dispersion minima (i.e., ‘velocity dispersion drops’) are common in our sample. We observe distinct dispersion drops in 11 out of 24 galaxies (46%). This is probably a lower limit considering the medium spatial resolution of our SAURON data. Only

4 of these 11 cases are known to have an active nucleus. Recent long-slit studies (Chung & Bureau 2004) revealed a velocity dispersion drop frequency of about 40% in a sample of 30 nearly edge-on S0-Sbc galaxies, which is consistent with our findings. The first observed cases of central velocity dispersion minima date back to the late 80s and early 90s (e.g., Bottema 1989, 1993; Fisher 1997). However, this subject has started to gain attention in the last years (e.g., Emsellem et al. 2001; Márquez et al. 2003). Despite the growth of observational examples, the nature of these drops is not well understood. First theoretical predictions for the presence of these velocity dispersion minima (Binney 1980) suggested that they were the natural consequence of inner regions of galaxies following an $r^{1/4}$ light profile (de Vaucouleurs 1948). Later on this prediction was extended to more general $r^{1/n}$ profiles (Sersic 1968) by Ciotti & Lanzoni (1997). In practice, these drops are not common in elliptical galaxies (Paper III). The objects in our sample are Sa galaxies with generally large bulges dominating the light in the inner regions. If bulges were scaled-down versions of ellipticals, then one would not expect velocity dispersion drops in Sa galaxies. Therefore, the observations lead to the picture that Sa bulges may have disk properties as well (Kormendy 1993). The latest N-body simulations associate the origin of these dispersion minima to kinematically cold components (i.e. discs), formed by gas inflow towards the central regions of the galaxy and subsequent star formation (Wozniak et al. 2003). However, the importance of dissipative processes (Bureau & Athanassoula 2005), and the role of bars (Heller & Shlosman 1994; Friedli & Benz 1995) is still unclear in this context.

A large fraction of the galaxies with sigma-drops do indeed show the presence of star formation at the same locations (as seen from the low [O III]/ $H\beta$ ratio). The presence of star formation in the inner regions of galaxies, however, does not always translate into a stellar velocity dispersion drop. Given the typical gas consumption time scale in normal disk galaxies (~ 1 Gyr), it is possible that many of the galaxies displaying these drops, but not young star formation, have simply used up all the available gas to form stars. The detection of the drop can also be more difficult due to the inclination of the galaxy, as in face-on configurations the contribution of the dynamically cold stars to the line-of-sight is much smaller than that of the surrounding bulge. Examples of this effect are found in NGC 4274 and NGC 4314. A more in-depth discussion of the link between the velocity dispersion drops and their underlying stellar populations will be the subject of a future paper in this series.

Some objects in the sample (NGC 2273, NGC 3623, NGC 4220, NGC 4245, NGC 4293, NGC 4369, NGC 4596, NGC 5448, NGC 5636) display misaligned photometric and kinematic axes, indicative of a non-axisymmetric structure (i.e., a bar). These misalignments are more easily detected at low galaxy inclinations, but it is still possible to recognise the existence of bars by means of their kinematic signatures even for edge-on configurations. Following the pioneering work of Kuijken & Merrifield (1995), recent N-body simulations of barred galaxies (Bureau & Athanassoula 2005) have suggested several bar diagnostics making use of the parameters of the Gauss-Hermite series (V , σ , h_3 , h_4). In our sample we find at least five highly-inclined galaxies (NGC 3623, NGC 4235, NGC 4274, NGC 5448, NGC 5689) that reveal some of the main kinematic signatures shown in the simulations: double-hump rotation curve, broad velocity dispersion profile with a plateau at moderate radii, and $h_3 - V$ correlation over the projected bar length. In addition to these bar diagnostics, other features such as boxy isophotes or cylindrical rotation hint at the presence of a bar in NGC 4220 and

NGC 4425. Nuclear star forming rings are also often interpreted in the context of bar driven evolution. We return to this point in Section 6.

5.2 Ionised-gas morphology and kinematics

As expected, nearly all the galaxies in our sample display significant amounts of ionised-gas emission. There are only two cases where the detection of ionised gas is marginal or absent (NGC 4425, NGC 6501). Similarly to the stellar kinematics, we can also correlate the presence and spatial morphology of the dust with the distribution seen in the SAURON ionised-gas maps. Dust features in the unsharp-masked images are usually associated with the presence of ionised-gas structures. However, the inverse is not always true. This may be due to the fact that dust is much more difficult to detect in face-on systems or is simply not there. The connection between ionised gas and dust is more evident in the $H\beta$ than in the [O III] emission, which overall also tends to be stronger than [O III]. This difference is particularly apparent in the [O III]/ $H\beta$ maps. A large fraction of the objects in our sample display very low [O III]/ $H\beta$ ratios, suggesting currently ongoing star formation. The morphology of star formation regions is varied. There are six cases in our sample where star formation occurs in ring-like structures (see Sect. 6). In some other galaxies, however, the star-forming regions spread across the main body of the galaxy (e.g., NGC 1056), align with strong dust lanes (e.g., NGC 4220) or have a more amorphous morphology (e.g., NGC 4369, NGC 4405). In most of the cases, these low [O III]/ $H\beta$ regions have gas velocity dispersion values below $\sim 50 \text{ km s}^{-1}$. This suggests that there is a large amount of cold gas present, from which stars have recently formed.

The velocity maps of the ionised gas in our sample are consistent with gas motions in a disc co-rotating with the stars. In these cases the rotational velocities exhibit rotation amplitudes larger than those of the stars, as expected from the dissipative nature of the gas (and the corresponding smaller asymmetric drift). A few cases depart from this simple description: NGC 4772 and NGC 5953, where the gas in certain regions rotates almost perpendicularly to the stars; NGC 7742, where the gas counter-rotates with respect to the stars; NGC 4383, which displays mean velocities confined in a jet-like structure; NGC 4369, that shows no well defined rotation axis, possibly due to the patchy nature of the gas distribution, and NGC 3623, where the gas traces spiral arm structure. Our maps also display differences in the $H\beta$ and [O III] mean velocities and velocity dispersions. This is particularly apparent in the inner arcseconds (e.g., NGC 4698, NGC 5475), and sometimes also outside the nuclear regions (e.g., NGC 5953, NGC 7742).

5.3 Misalignments

The measurement of misalignments between structural components in early-type galaxies has often been used to assess the frequency of triaxiality, by measuring differences between the photometric and kinematic major axes (e.g., Binney 1985; Franx et al. 1991), or to determine the occurrence of accretion events, by measuring the misalignment between the kinematics of the stellar and gaseous component (e.g., Kannappan & Fabricant 2001). Here, we measure both types of misalignments to quantify the presence of bars or triaxial bulges and the presence of decoupled gaseous components in our sample, and to investigate their dependence on environment.

We determined the photometric major axis of each galaxy by computing the weighted second moments of the intensity distribution using the large scale ground-based MDM images (see Sect. 2).

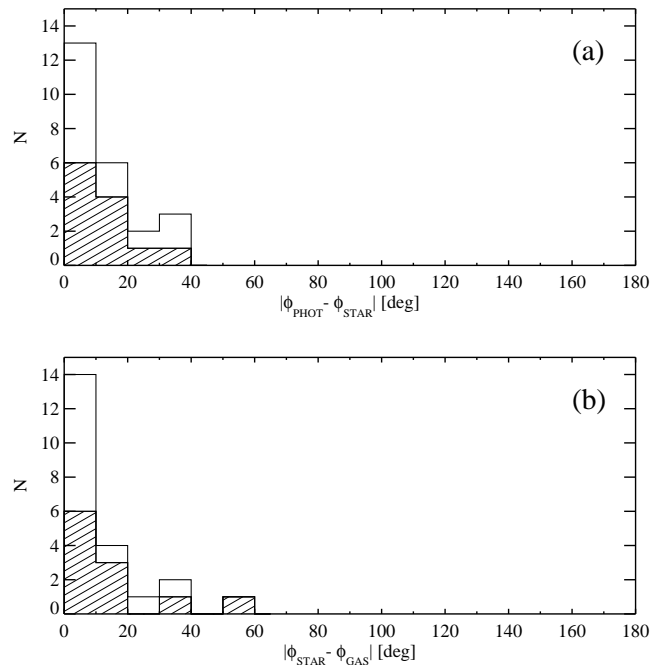


Figure 4. Distribution of misalignments in our sample of galaxies. (a) misalignment between the photometric and stellar kinematic major axes. (b) misalignment between the stellar and gaseous kinematic major axes. In both panels the solid line represents the distribution for the whole sample, while the shaded area shows the distribution for field galaxies only.

This generally corresponds to the position angle of the main disc. We used the MDM images in the F814W filter to minimise the effects of dust in the determination of the photometric major axis. The stellar and gaseous kinematic major axes were obtained by finding the position angle that minimised the difference between the SAURON velocity fields and a bi-antisymmetric representation of the velocity field (see Appendix C in Krajnović et al. 2006). Both methods are robust indicators that provide a good estimate of the *global* position angle of the maps used, and thus peculiarities on small scales are not visible in the final distribution of misalignments. The values of the measured misalignments are listed in Table 2.

The study of triaxiality due to past merging events is difficult to assess in our sample of disc galaxies. Spiral galaxies are known to suffer disc instabilities that could eventually lead to the formation of bars (i.e., internal triaxial bodies). With time, it is likely that the evolution of the bar will erase any signature of triaxiality from any previous merging event. Despite the progress in this field, the relative importance of internal versus external processes and their role on the formation of spiral galaxies is not well established yet (see Kormendy & Kennicutt 2004 for a review on the subject).

In Figure 4(a), we quantify the degree of misalignment between the stellar surface brightness distribution with respect to the main stellar rotation axis for each galaxy. The histogram displays a gradually increasing number of galaxies towards small misalignments. As discussed in § 5.1, bars are, at least in part, responsible for the spread towards intermediate misalignments. However, in the figure, barred galaxies alone do not account for the observed excess of galaxies at intermediate values. The presence of dust in many of the galaxies in our sample plays an important role in the observed distribution. No significant difference is found between field and

cluster members. A KS-test indicates that there is a 78% probability that the distributions of the two classes are identical.

Figure 4(b) presents a histogram with the observed misalignments between the kinematics of the stars and ionised gas. Similarly to panel 4(a) there is an excess of galaxies with small misalignments. The spread towards intermediate misalignments seems to be due to non-circular motions in the ionised-gas velocity fields (e.g., NGC 5448, Fathi et al. 2005), and to a lesser extent by dust extinction. From these figures, the misalignment distribution appears to be consistent for field and cluster galaxies (KS-test, $p=73\%$). The only two galaxies without ionised-gas detection, NGC 4425 and NGC 6501, belong to cluster and field environments, respectively.

These results contrast with our findings for early-type galaxies (Paper V), as there are no cases displaying misalignments above 60° in our sample. The absence of counter-rotating gas and stars or of gas minor-axis rotation in our sample is consistent with the finding of previous surveys (e.g., Kannappan & Fabricant 2001) that such phenomena are exceedingly rare in spiral galaxies. A likely explanation for the observed distribution is that in the event of an accretion of a small satellite by a spiral galaxy, the axisymmetric geometry of the system will cause the accreted material to quickly settle on the main galactic plane, where pre-existing gas would shock with counter-rotating accreted gas, dissipating its angular momentum or inducing star formation (see also Rix et al. 1995; Corsini et al. 1998; Haynes et al. 2000; Kannappan & Fabricant 2001, and references therein).

6 STAR FORMATION IN SA BULGES

Determining the rate at which stars are born in galaxies is key to understanding how galaxies form and evolve. Since the first estimates of star-formation rates using colors (e.g., Tinsley 1968), many different diagnostics have been proposed to measure the amount of stellar mass produced in a given time (i.e., ultraviolet continuum, recombination lines, forbidden lines, far-infrared continuum). See Kennicutt (1998) for an extensive review on this subject.

In this section we use one of the most widely applied diagnostics to determine the importance of the star formation rate (SFR) in our sample of galaxies: the SFR– $H\alpha$ luminosity relation. We use the prescription of Kennicutt (1998):

$$\text{SFR}(M_\odot \text{ yr}^{-1}) = \frac{L(H\alpha)}{7.9 \times 10^{42} \text{ erg s}^{-1}} \quad (1)$$

The wavelength range covered by SAURON does not allow for a direct measurement of the $H\alpha$ luminosity, but $H\beta$ fluxes instead. We used the measured Hubble flow⁴, listed in Table 2, to convert our observed $H\beta$ fluxes into luminosities. Given that many galaxies in our sample display significant amounts of dust, we corrected those $H\beta$ luminosities for dust attenuation. For the galactic extinction we used the correction factors in V -band of Schlegel et al. (1998) as given by the NED database. We also considered the expected dust extinction of each galaxy due to its inclination. For that we used the values listed in the Hyperleda catalogue, which were determined using the prescription of Bottinelli et al. (1995). The values, originally in B -band, were converted to V -band assuming the attenuation law of Cardelli et al. (1989). After these corrections, we converted the extinction corrected $H\beta$ luminosities to $H\alpha$ luminosities using the theoretical conversion factor 2.86 (Osterbrock 1989). The SFR was then determined using the equation above. Finally, we derived the

⁴ $H_0=71 \text{ km s}^{-1} \text{ Mpc}^{-1}$ (Bennett et al. 2003).

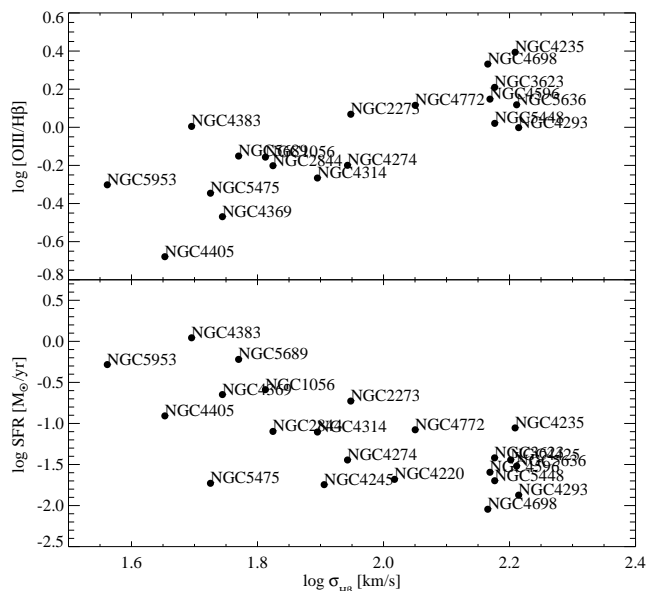


Figure 5. $[O\ III]/H\beta$ ratio and star-formation rate versus $H\beta$ velocity dispersion. Galaxies displaying low velocity dispersions also show the lowest values of $[O\ III]/H\beta$, suggesting a link between the level of star formation and the dynamical state of the gas. This is confirmed in the bottom panel where the higher star formation rates are found in galaxies with lowest $H\beta$ velocity dispersion.

masses of the ionised gas in each galaxy following Kim (1989) and assuming a Case B recombination at $T=10,000\text{K}$ with an electron density of $n = 100 \text{ cm}^{-3}$ (Osterbrock 1989). Table 2 lists the values of the observed $H\beta$ fluxes, correction factors for dust extinction, computed extinction corrected $H\alpha$ luminosities, star formation rates and ionised-gas masses within the SAURON FoV.

Following the investigation of the relation between star formation and low ionised-gas velocity dispersions in sigma-drops in §5.1, we looked at whether a similar empirical relation holds in general in our sample. In Figure 5 we plot $[O\ III]/H\beta$ ratio and SFR versus the $H\beta$ velocity dispersion for each galaxy. The $[O\ III]/H\beta$ ratio is the average over the SAURON FoV, while the SFR is the total over the same area. The $H\beta$ velocity dispersion is the luminosity weighted average of the individual measurements over the full SAURON map for each galaxy. We find that ionised-gas velocity dispersion values are low ($\sim 50 \text{ km s}^{-1}$) in regions where the $[O\ III]/H\beta$ ratio is also low (≤ 1 , see Fig.5, top panel). Galaxies displaying the largest SFR are also those showing the lowest $H\beta$ velocity dispersions (see Fig.5, bottom panel). The obvious interpretation is that we are seeing stars being formed from cold (i.e., low velocity dispersion) gas. A similar behaviour is found in SAURON observations of the grand-design spiral galaxy M 100 (Allard et al. 2005) and GMOS IFU observations of NGC 1097 (Fathi et al. 2006). The relation, although still present, becomes much weaker if the $[O\ III]$ velocity dispersion is used instead, displaying the limitations of the $[O\ III]$ line as an indicator of star formation.

The star formation rates found here range over several orders of magnitude and appear to be in good agreement with those for normal disc galaxies (Kennicutt 1998). Some of the most extreme cases of star formation in our sample appear in the form of circumnuclear star-forming rings. In total we have detected six (NGC 2844, NGC 4245, NGC 4274, NGC 4314, NGC 5953, NGC 7742) in our sample of 24 galaxies, which is consistent

with the most recent estimates from H α studies of larger samples ($21\pm 5\%$, Knapen 2005). The formation of star-forming rings is usually associated with the interplay between bar-driven inflow and bar resonances (Schwarz 1984; Byrd et al. 1994; Piner et al. 1995). In our sample there are three galaxies, displaying inner rings, that are indeed classified as barred (NGC 4245, NGC 4274, NGC 4314). Star-forming rings in general, however, do not need to be accompanied by the visible presence of a bar. As gas in galaxies is very sensitive to non-axisymmetric structures, a simple oval (i.e. weak bar) suffices to force the re-distribution of the gas (i.e., Buta & Combes 1996). NGC 7742 (see also Paper II) could be an example of this scenario, where there is no clear evidence of a bar. This hypothesis is further supported by the presence of a central decoupled component in the inner parts of the galaxy which, as discussed in Section 5, is common in barred galaxies. However, given the striking resemblance of NGC 7742 to Hoag's Object (Schweizer et al. 1987), alternative formation scenarios may include an interaction event with a neighbour galaxy (Toomre 1977; Horellou & Combes 2001). In this context, the star-forming ring in NGC 2844 may be the consequence of an interaction with the nearby galaxies (e.g., NGC 2852, NGC 2853, see Appendix A). An even more evident case of the interacting scenario is the close pair formed by NGC 5953 and NGC 5954. In this case, the star-forming ring in NGC 5953 is co-spatial with the kinematically decoupled component seen in the stellar and gas kinematics (§5.1, §5.2), thus indicating that we may be witnessing the formation of a decoupled component as a result of an ongoing interaction.

7 CONCLUDING REMARKS

The maps presented in this paper constitute a systematic study of the stellar and ionised-gas morphology and kinematics of a representative sample of 24 Sa galaxies in the nearby universe. Our analysis reveals stellar kinematically decoupled components in 12 of the galaxies in our sample. Many of them show additional velocity dispersion drops, which are often associated with the presence of young stars. The ionised gas is almost ubiquitous in our sample and is, in general, accompanied by the presence of dust. The kinematics of the gas is consistent with circular rotation in a disc co-rotating with respect to the stars. We assessed the importance of triaxiality and interactions by studying the distribution of misalignments between the photometric and stellar kinematics major axes, and also between the stellar and gas kinematic major axes. We concluded that, even though dust contamination plays an important role, bars are the main source for the observed non-axisymmetry in our sample. There is also no evidence for major accretion events in our sample, except in NGC 4698, and NGC 5953. Derived star formation rates appear to be in good agreement with previous work in the literature. In general, star formation is intense in many galaxies and displays varied morphologies; the most striking cases being six galaxies showing circumnuclear star-forming rings. We related the origin of these rings to gas redistribution by bars or ovals (e.g., NGC 4314, NGC 7742), or to interaction events (e.g., NGC 5953).

The maps and analysis shown here comprise only part of the information that can be extracted from the SAURON data. A more detailed analysis and interpretation of some of the issues raised in this paper (i.e. including an in-depth study of the stellar populations of these objects) will be the subject of a forthcoming paper in this series.

ACKNOWLEDGMENTS

We would like to thank John Beckman and Almudena Zurita for very useful discussions during the course of this paper, and also Katia Ganda and Glenn van de Ven for their comments and a careful reading of the manuscript. We are grateful to the referee, Daniel Thomas, for useful suggestions that have helped to improve the presentation of the main results of the paper. We thank the Isaac Newton Group staff, in particular Rene Rутten, Tom Gregory and Chris Benn, for enthusiastic and competent support on La Palma. JFB acknowledges support from the Euro3D Research Training Network, funded by the EC under contract HPRN-CT-2002-00305. MC acknowledges support from a VENI grant 639.041.203 awarded by the Netherlands Organization for Scientific Research (NWO). KF acknowledges financial support from the Wenner-Gren Foundations. The SAURON project is made possible through grants 614.13.003, 781.74.203, 614.000.301 and 614.031.015 from NWO and financial contributions from the Institut National des Sciences del'Univers, the Université Claude Bernard Lyon I, the Universities of Durham, Leiden, and Oxford, the British Council, PPARC grant 'Extragalactic Astronomy & Cosmology at Durham 1998–2002', and the Netherlands Research School for Astronomy NOVA. RLD is grateful for the award of a PPARC Senior Fellowship (PPA/Y/S/1999/00854) and postdoctoral support through PPARC grant PPA/G/S/2000/00729. This project made use of the HyperLeda and NED databases. The Digitized Sky Surveys were produced at the Space Telescope Science Institute under U.S. Government grant NAG W-2166. The images of these surveys are based on photographic data obtained using the Oschin Schmidt Telescope on Palomar Mountain and the UK Schmidt Telescope.

REFERENCES

- Afanasiev V. L., Sil'chenko O. K., 2005, *A&A*, 429, 825
 Allard E. L., Peletier R. F., Knapen J. H., 2005, *ApJ*, 633, L25
 Asif M. W., Mundell C. G., Pedlar A., 2005, *MNRAS*, 359, 408
 Bacon R., et al., 2001, *MNRAS*, 326, 23 [Paper I]
 Balcells M., Peletier R. F., 1994, *AJ*, 107, 135
 Benedict G. F., Higdon J. L., Tollestrup E. V., Hahn J. M., Harvey P. M., 1992, *AJ*, 103, 757
 Benedict G. F., Smith B. J., Kenney J. D. P., 1996, *AJ*, 112, 1318
 Bennett C. L., et al., 2003, *ApJS*, 148, 97
 Bernardi M., Alonso M. V., da Costa L. N., Willmer C. N. A., Wegner G., Pellegrini P. S., Rité C., Maia M. A. G., 2002, *AJ*, 123, 2990
 Bertola F., Corsini E. M., Vega Beltrán J. C., Pizzella A., Sarzi M., Cappellari M., Funes J. G., 1999, *ApJ*, 519, L127
 Binney J., 1980, *MNRAS*, 190, 873
 Binney J., 1985, *MNRAS*, 212, 767
 Bottema R., 1989, *A&A*, 221, 236
 Bottema R., 1993, *A&A*, 275, 16
 Bottinelli L., Gouguenheim L., Paturel G., Teerikorpi P., 1995, *A&A*, 296, 64
 Bureau M., Athanassoula E., 2005, *ApJ*, 626, 159
 Buta R., Combes F., 1996, *Fundamentals of Cosmic Physics*, 17, 95
 Byrd G., Rautiainen P., Salo H., Buta R., Crocher D. A., 1994, *AJ*, 108, 476
 Cappellari M., Copin Y., 2003, *MNRAS*, 342, 345
 Cappellari M., Emsellem E., 2004, *PASP*, 116, 138
 Cardelli J. A., Clayton G. C., Mathis J. S., 1989, *ApJ*, 345, 245
 Chemin L., et al., 2005, *A&A*, 436, 469

- Chemin L., et al., 2006, MNRAS, 366, 812
- Chromey F. R., Elmegreen D. M., Mandell A., McDermott J., 1998, AJ, 115, 2331
- Chung A., Bureau M., 2004, AJ, 127, 3192
- Cid Fernandes R., et al., 2004, ApJ, 605, 105
- Ciotti L., Lanzoni B., 1997, A&A, 321, 724
- Corsini E. M., Pizzella A., Coccato L., Bertola F., 2003, A&A, 408, 873
- Corsini E. M., Pizzella A., Funes J. G., Vega Beltran J. C., Bertola F., 1998, A&A, 337, 80
- de Vaucouleurs G., 1948, Annales d'Astrophysique, 11, 247
- de Zeeuw P. T., et al., 2002, MNRAS, 329, 513 [Paper II]
- di Nella H., Garcia A. M., Garnier R., Paturel G., 1995, A&AS, 113, 151
- Emsellem E., et al., 2004, MNRAS, 352, 721 [Paper III]
- Emsellem E., Greusard D., Combes F., Friedli D., Leon S., Pécontal E., Wozniak H., 2001, A&A, 368, 52
- Erwin P., 2004, A&A, 415, 941
- Erwin P., Sparke L. S., 2003, ApJS, 146, 299
- Eskridge P. B., et al., 2002, ApJS, 143, 73
- Falcón-Barroso J., Balcells M., Peletier R. F., Vazdekis A., 2003, A&A, 405, 455
- Fathi K., van de Ven G., Peletier R., Emsellem E., Falcón-Barroso J., Cappellari M., de Zeeuw P., 2005, MNRAS, 364, 773
- Fathi K., Storch-Bergmann T., Riffel R. A., Winge C., Axon D. J., Robinson A., Capetti A., Marconi A., 2006, ApJ, in press
- Ferruit P., Binette L., Sutherland R. S., Pecontal E., 1997, A&A, 322, 73
- Ferruit P., Wilson A. S., Mulchaey J., 2000, ApJS, 128, 139
- Fisher D., 1997, AJ, 113, 950
- Franx M., Illingworth G., de Zeeuw T., 1991, ApJ, 383, 112
- Friedli D., Benz W., 1995, A&A, 301, 649
- Ganda K., Falcón-Barroso J., Peletier R. F., Cappellari M., Emsellem E., McDermid R. M., de Zeeuw P. T., Carollo C. M., 2006, MNRAS, in press (astro-ph/0512304)
- Gerhard O. E., 1993, MNRAS, 265, 213
- Gerssen J., Kuijken K., Merrifield M. R., 1999, MNRAS, 306, 926
- Giuricin G., Marinoni C., Ceriani L., Pisani A., 2000, ApJ, 543, 178
- Gonzalez Delgado R. M., Perez E., 1996, MNRAS, 281, 781
- Gonzalez Delgado R. M., Perez E., Tadhunter C., Vilchez J. M., Rodriguez-Espinosa J. M., 1997, ApJS, 108, 155
- Goudfrooij P., Emsellem E., 1996, A&A, 306, L45
- Hameed S., Devereux N., 2005, AJ, 129, 2597
- Haynes M. P., Jore K. P., Barrett E. A., Broeils A. H., Murray B. M., 2000, AJ, 120, 703
- Heller C. H., Shlosman I., 1994, ApJ, 424, 84
- Hernández-Toledo H. M., Fuentes-Carrera I., Rosado M., Cruz-González I., Franco-Balderas A., Dultzin-Hacyan D., 2003, A&A, 412, 669
- Ho L. C., Filippenko A. V., Sargent W. L., 1995, ApJS, 98, 477
- Ho L. C., Filippenko A. V., Sargent W. L. W., 1997a, ApJS, 112, 315
- Ho L. C., Filippenko A. V., Sargent W. L. W., Peng C. Y., 1997b, ApJS, 112, 391
- Horellou C., Combes F., 2001, Ap&SS, 276, 1141
- Jenkins C. R., 1984, ApJ, 277, 501
- Jiménez-Benito L., Díaz A. I., Terlevich R., Terlevich E., 2000, MNRAS, 317, 907
- Kannappan S. J., Fabricant D. G., 2001, AJ, 121, 140
- Kennicutt R. C., 1998, ARA&A, 36, 189
- Kim D.-W., 1989, ApJ, 346, 653
- Knapen J. H., 2005, A&A, 429, 141
- Koopmann R. A., Kenney J. D. P., 2004, ApJ, 613, 866
- Kormendy J., 1993, in IAU Symp. 153: Galactic Bulges Kinematics of extragalactic bulges: evidence that some bulges are really disks. p. 209
- Kormendy J., Kennicutt R. C., 2004, ARA&A, 42, 603
- Krajnović D., Cappellari M., de Zeeuw P., Copin Y., 2006, MNRAS, 366, 787
- Kuijken K., Merrifield M. R., 1995, ApJ, 443, L13
- Kuntschner H., et al., 2006, MNRAS, in press [Paper VI] (astro-ph/0602192)
- Lütticke R., Dettmar R.-J., Pohlen M., 2000, A&AS, 145, 405
- Landsman W. B., 1993, in ASP Conf. Ser. 52: Astronomical Data Analysis Software and Systems II The IDL Astronomy User's Library. p. 246
- Laurikainen E., Salo H., 2002, MNRAS, 337, 1118
- Márquez I., Masegosa J., Durret F., González Delgado R. M., Moles M., Maza J., Pérez E., Roth M., 2003, A&A, 409, 459
- Osterbrock D. E., 1989, Astrophysics of gaseous nebulae and active galactic nuclei. University Science Books, 1989, p. 422
- Pérez-Ramírez D., Knapen J. H., Peletier R. F., Laine S., Doyon R., Nadeau D., 2000, MNRAS, 317, 234
- Peletier R. F., Knapen J. H., Shlosman I., Pérez-Ramírez D., Nadeau D., Doyon R., Rodriguez Espinosa J. M., Pérez García A. M., 1999, ApJS, 125, 363
- Piner B. G., Stone J. M., Teuben P. J., 1995, ApJ, 449, 508
- Pizzella A., Corsini E. M., Morelli L., Sarzi M., Scarlata C., Stiavelli M., Bertola F., 2002, ApJ, 573, 131
- Plana H., Boulesteix J., Amram P., Carignan C., Mendes de Oliveira C., 1998, A&AS, 128, 75
- Press W. H., Teukolsky S. A., Vetterling W. T., Flannery B. P., 1992, Numerical recipes in FORTRAN. The art of scientific computing. Cambridge: University Press, c1992, 2nd ed.
- Prugniel P., Simien F., 1996, A&A, 309, 749
- Rampazzo R., Reduzzi L., Sulentic J. W., Madejsky R., 1995, A&AS, 110, 131
- Reshetnikov V. P., 1993, A&A, 280, 400
- Rix H.-W. R., Kennicutt R. C., Braun R., Walterbos R. A. M., 1995, ApJ, 438, 155
- Rubin V. C., Waterman A. H., Kenney J. D. P., 1999, AJ, 118, 236
- Sarzi M., Corsini E. M., Pizzella A., Vega Beltrán J. C., Cappellari M., Funes J. G., Bertola F., 2000, A&A, 360, 439
- Sarzi M., et al. 2005, MNRAS, 366, 1151 [Paper V]
- Schlegel D. J., Finkbeiner D. P., Davis M., 1998, ApJ, 500, 525
- Schwarz M. P., 1984, MNRAS, 209, 93
- Schweizer F., Ford W. K. J., Jederzejewski R., Giovanelli R., 1987, ApJ, 320, 454
- Sersic J. L., 1968, Atlas de Galaxias Australes. Cordoba, Argentina: Observatorio Astronomico.
- Shaw M., Axon D., Probst R., Gatley I., 1995, MNRAS, 274, 369
- Sofue Y., Tomita A., Tutui Y., Honma M., Takeda Y., 1998, PASJ, 50, 427
- Terlevich E., Diaz A. I., Terlevich R., 1990, MNRAS, 242, 271
- Tinsley B. M., 1968, ApJ, 151, 547
- Toomre A., 1977, p. 401
- Usui T., Saito M., Tomita A., 1998, AJ, 116, 2166
- van der Marel R. P., Franx M., 1993, ApJ, 407, 525
- Vazdekis A., 1999, ApJ, 513, 224
- Veilleux S., Kim D.-C., Sanders D. B., Mazzarella J. M., Soifer B. T., 1995, ApJS, 98, 171
- Wozniak H., Combes F., Emsellem E., Friedli D., 2003, A&A, 409, 469

Yoshida M., Yamada T., Kosugi G., Taniguchi Y., Mouri H., 1993,
PASJ, 45, 761

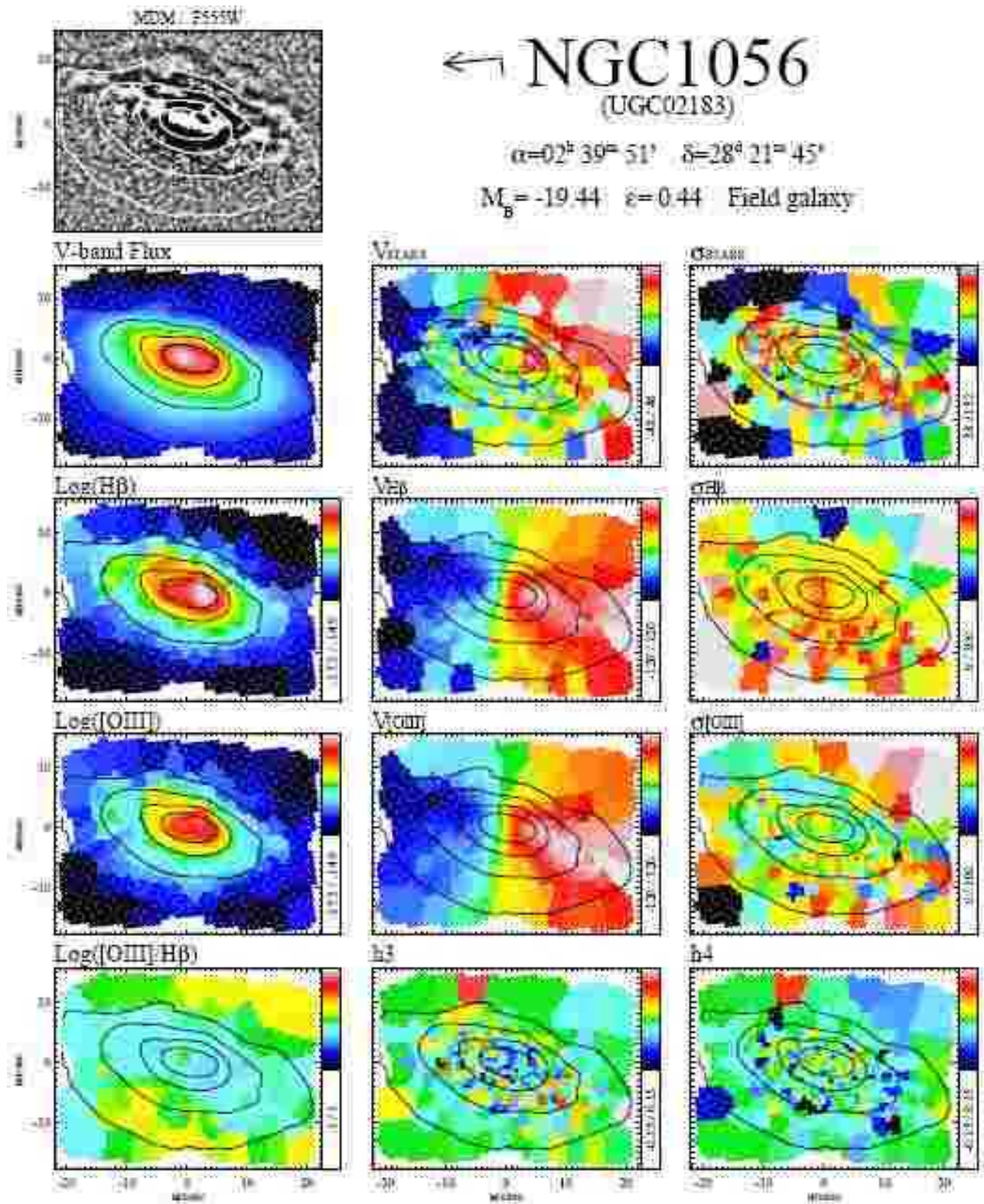


Figure 6a. Maps of the stellar and ionised-gas distribution and kinematics of the 24 Sa galaxies in the SAURON representative sample. The SAURON spectra have been spatially binned to a minimum signal-to-noise of 60 by means of the Voronoi 2D-binning algorithm of Cappellari & Copin (2003). The arrow and its associated dash at the top of each figure mark the North and East directions, respectively; the corresponding position angle of the vertical (upward) axis is provided in Table 2. *First row:* HST or ground-based unsharp-masked image. *Second row:* (i) reconstructed total intensity (in mag/arcsec² with an arbitrary zero point), (ii) stellar mean velocity V , and (iii) stellar velocity dispersion σ (in km s⁻¹). *Third row:* (i) H β flux (in logarithmic scale), (ii) mean radial velocity, and (iii) velocity dispersion (in km s⁻¹). *Fourth row:* as *third row* for the [O III] line. *Fifth row:* (i) [O III]/H β ratio map (in logarithmic scale), (ii) and (iii) Gauss–Hermite moments h_3 and h_4 . The cuts levels are indicated in a box on the right hand side of each map. Those bins in the ionised-gas maps with A/N below the thresholds stated in the text are colored in dark grey.

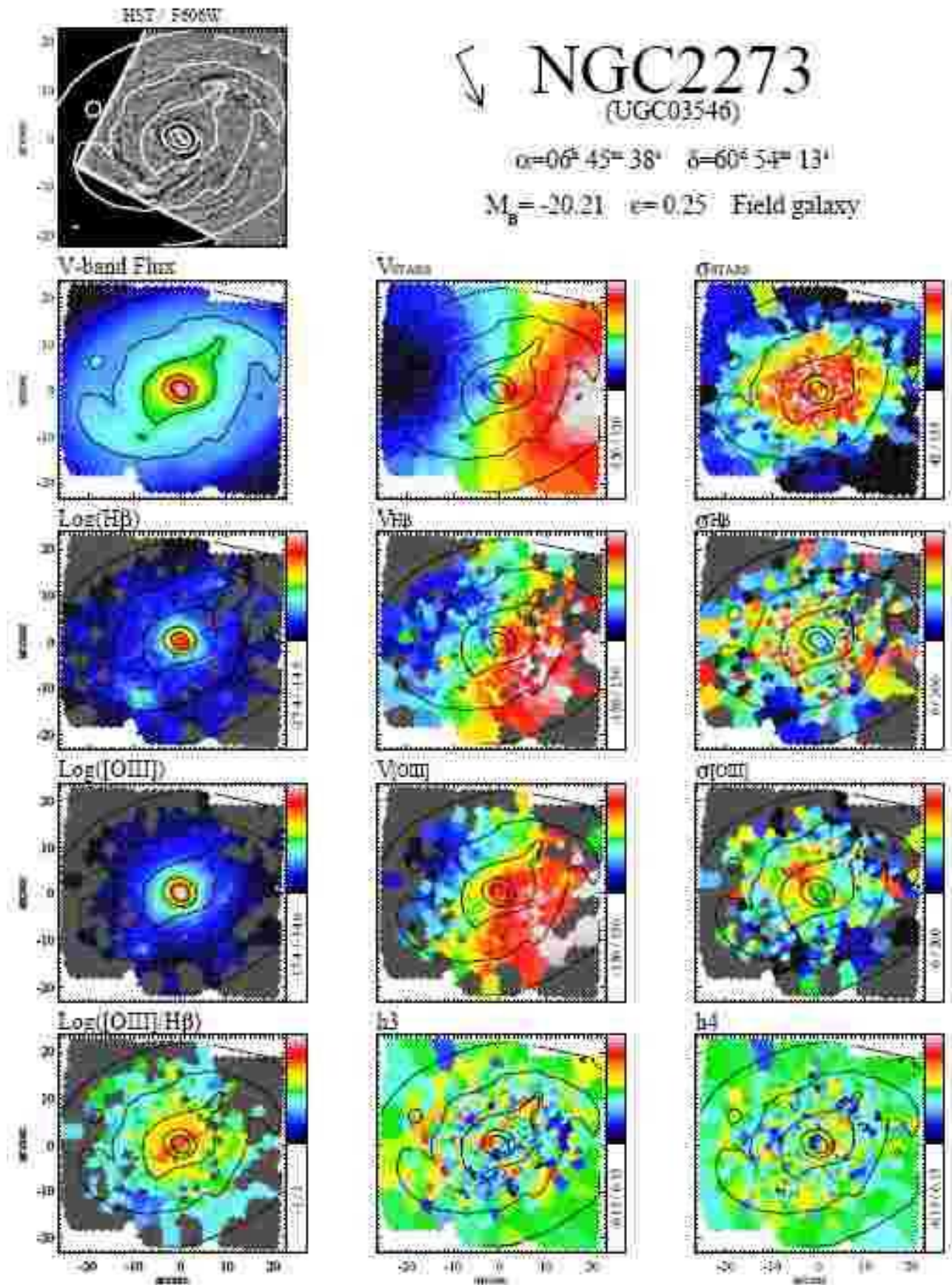


Figure 6b.

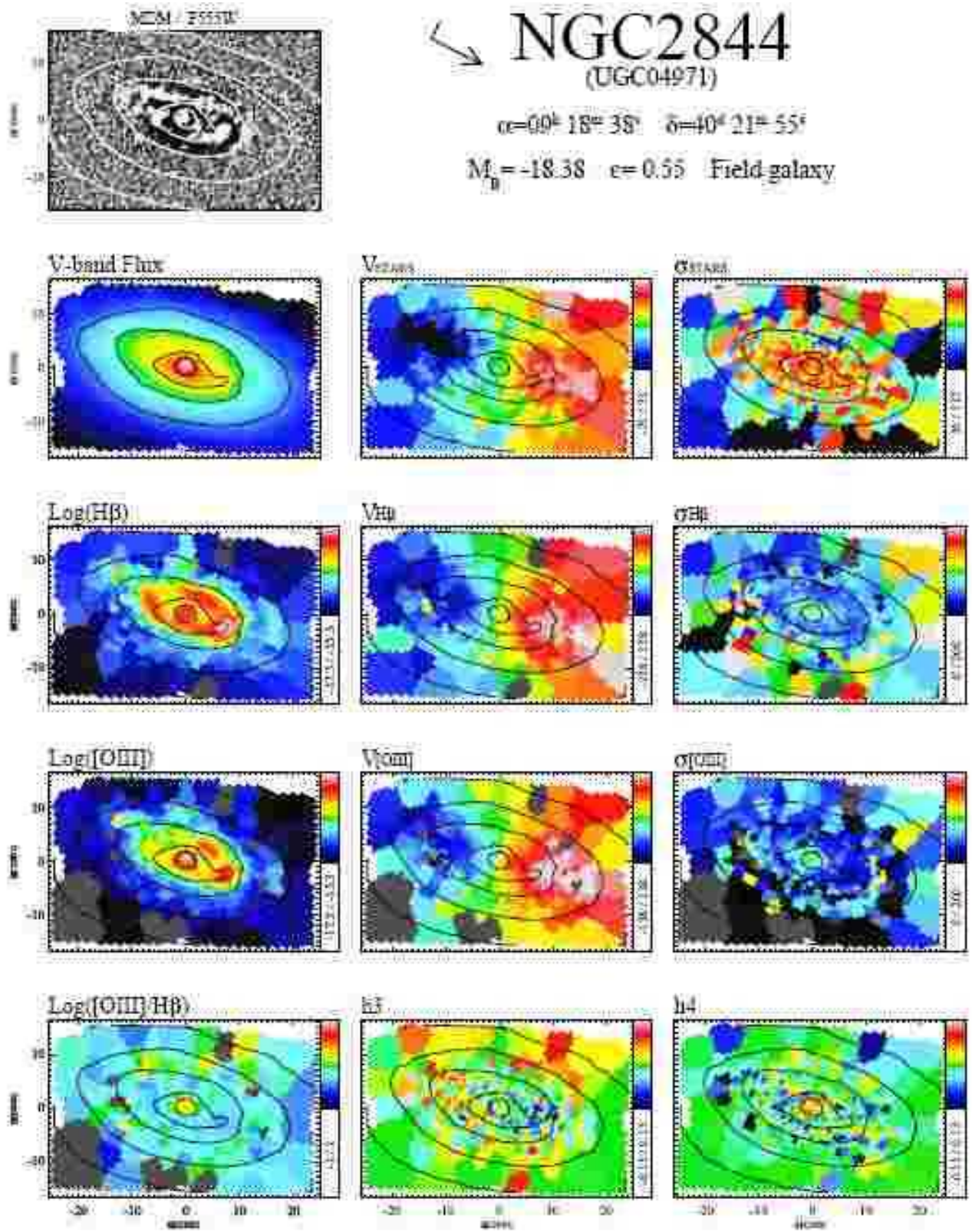


Figure 6c.

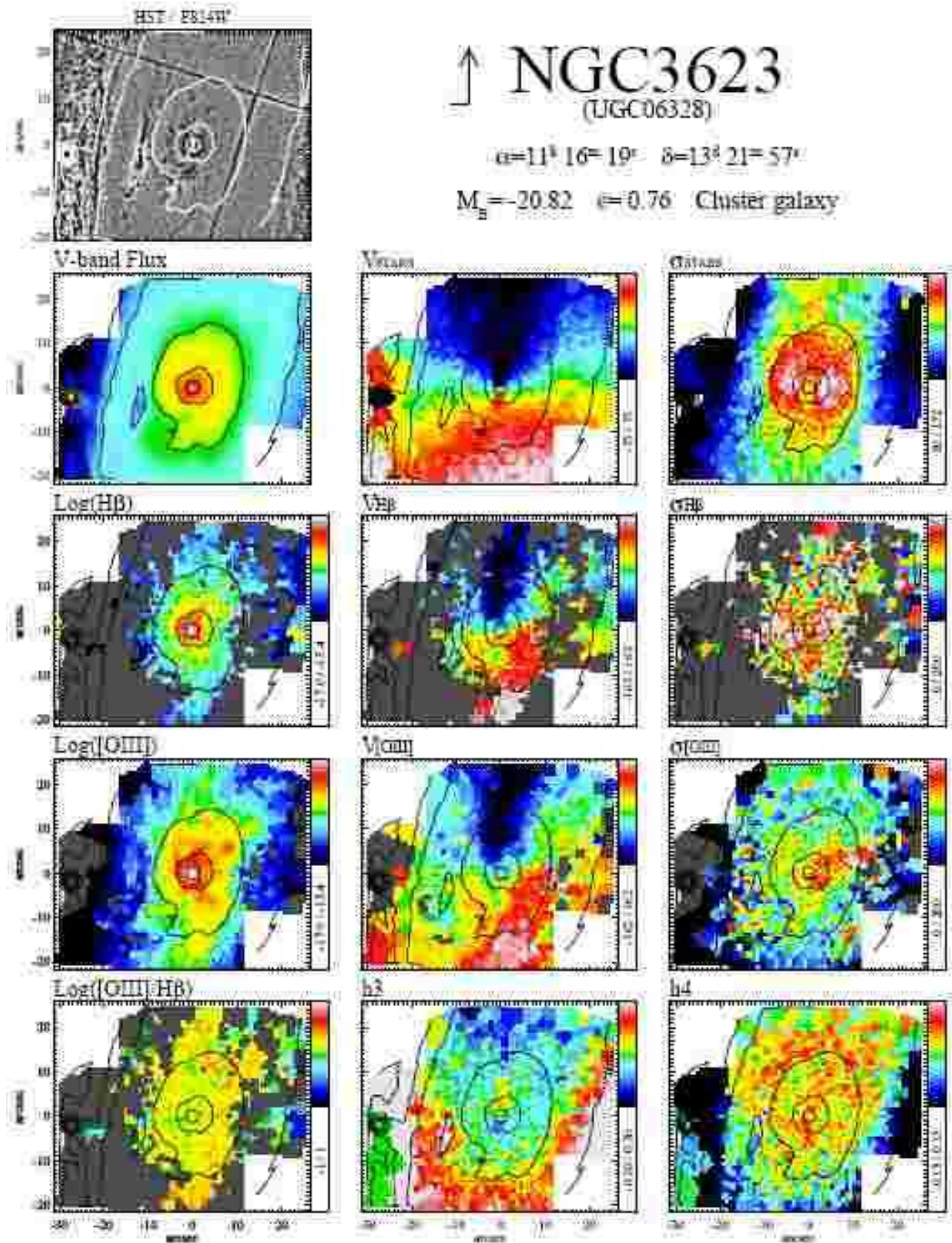


Figure 6d.

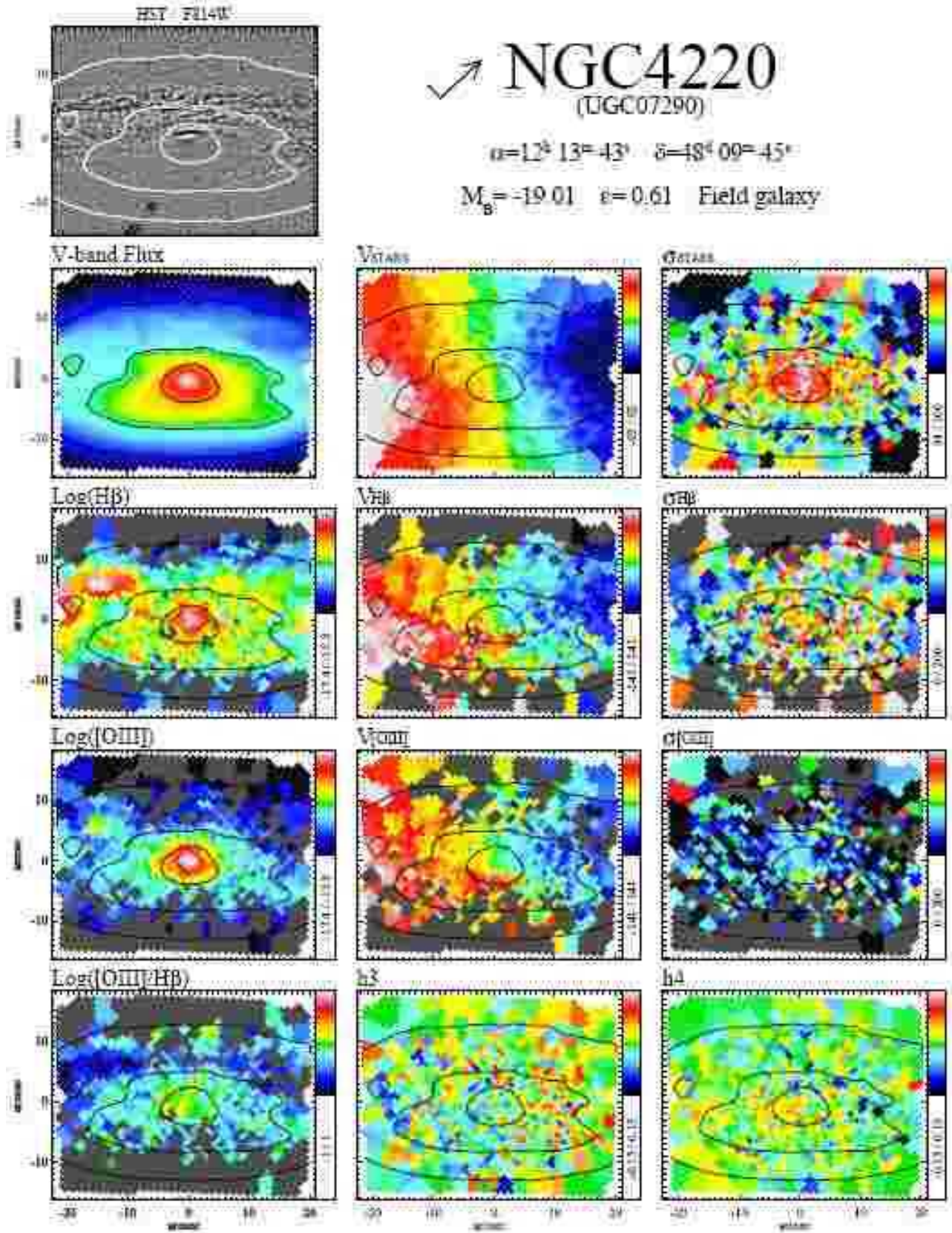


Figure 6e.

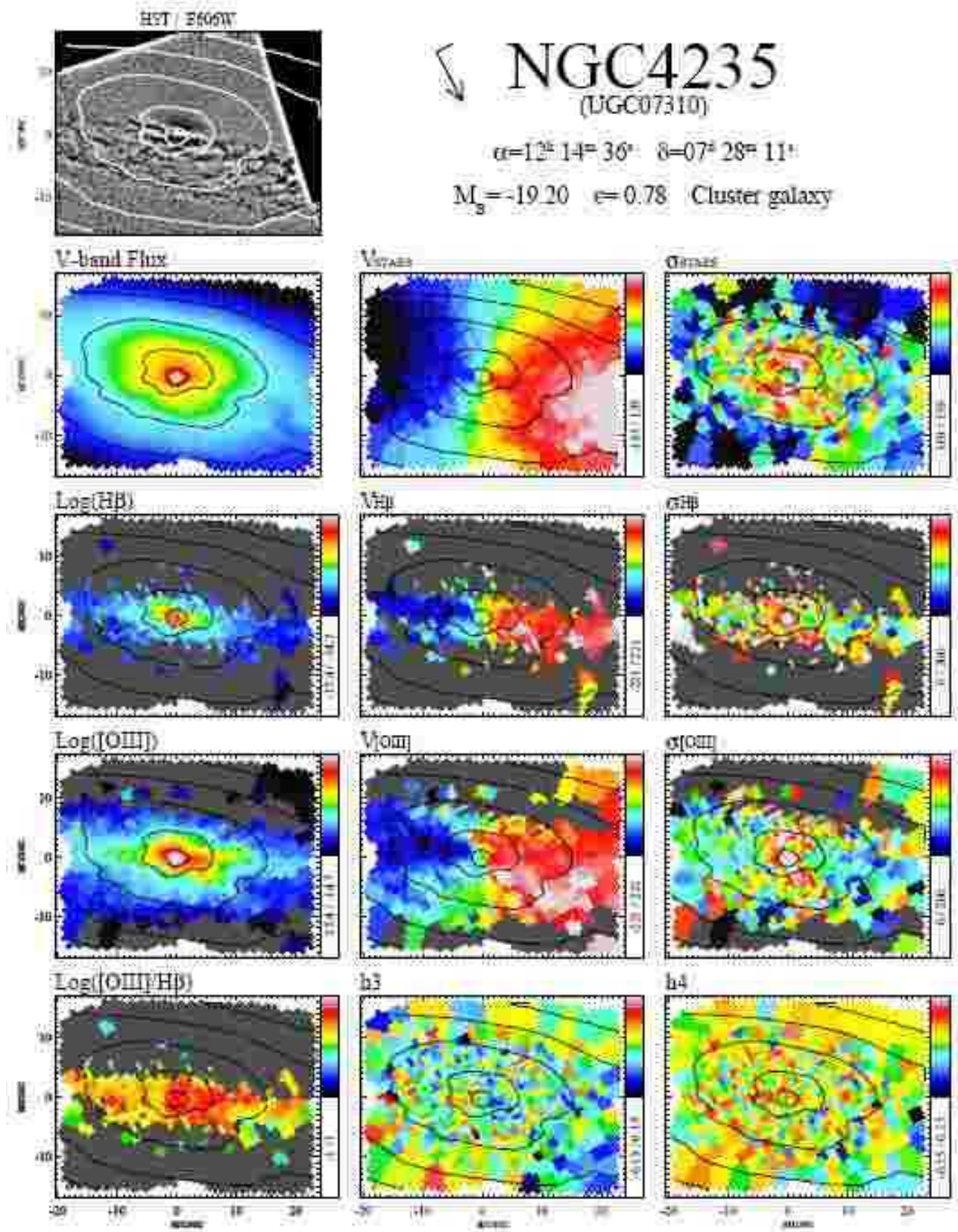


Figure 6f.

Figure 6f.

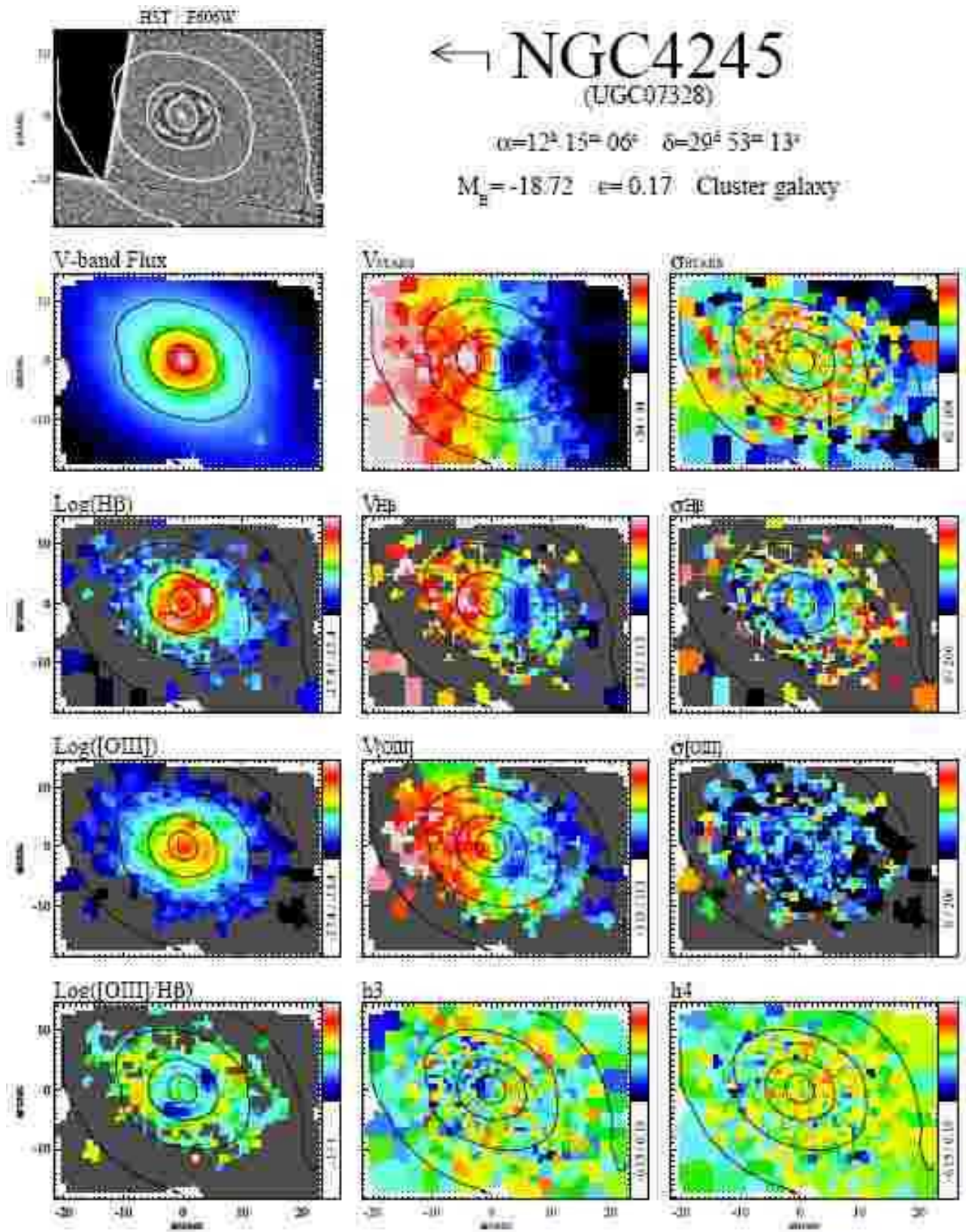


Figure 6.

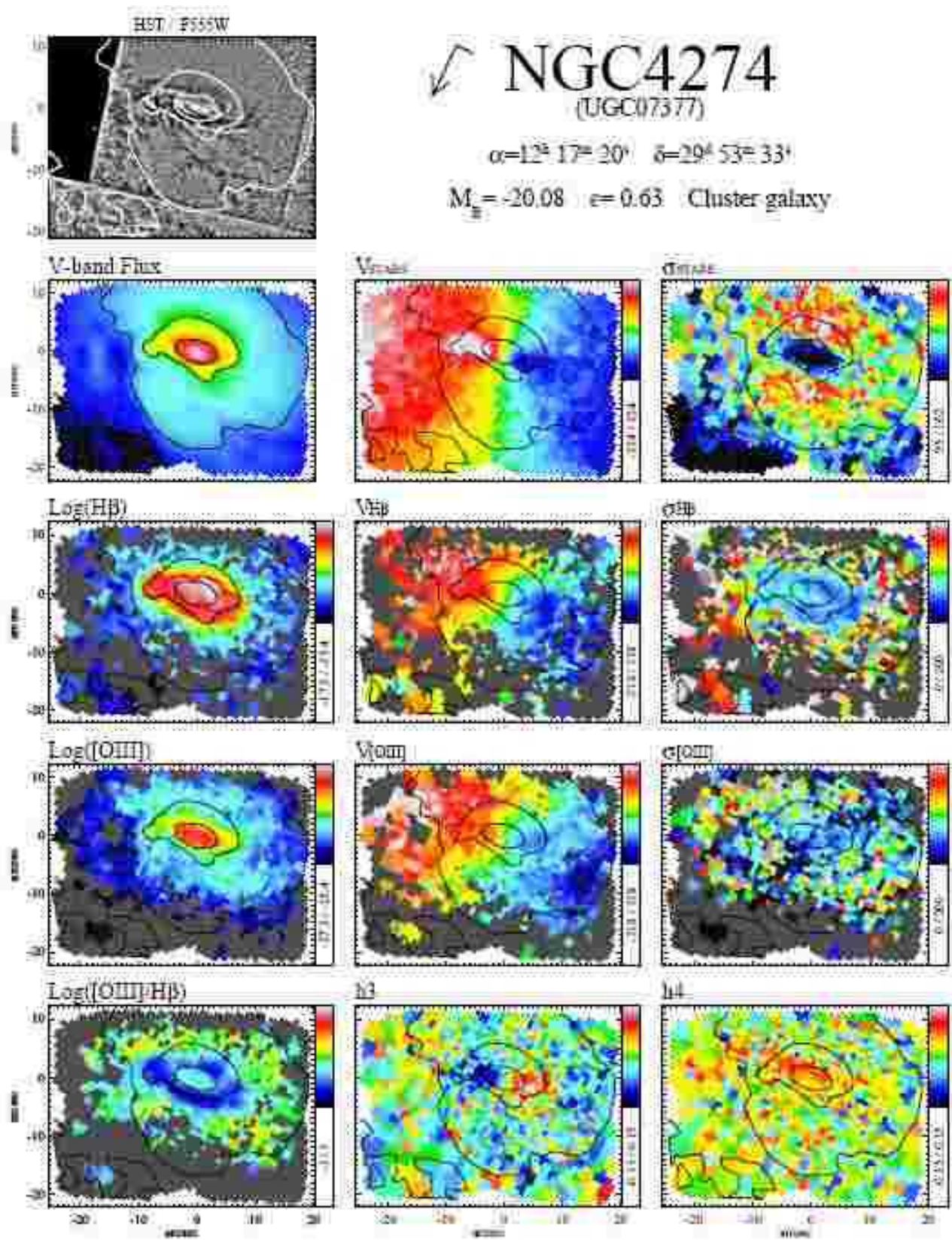


Figure 6h.

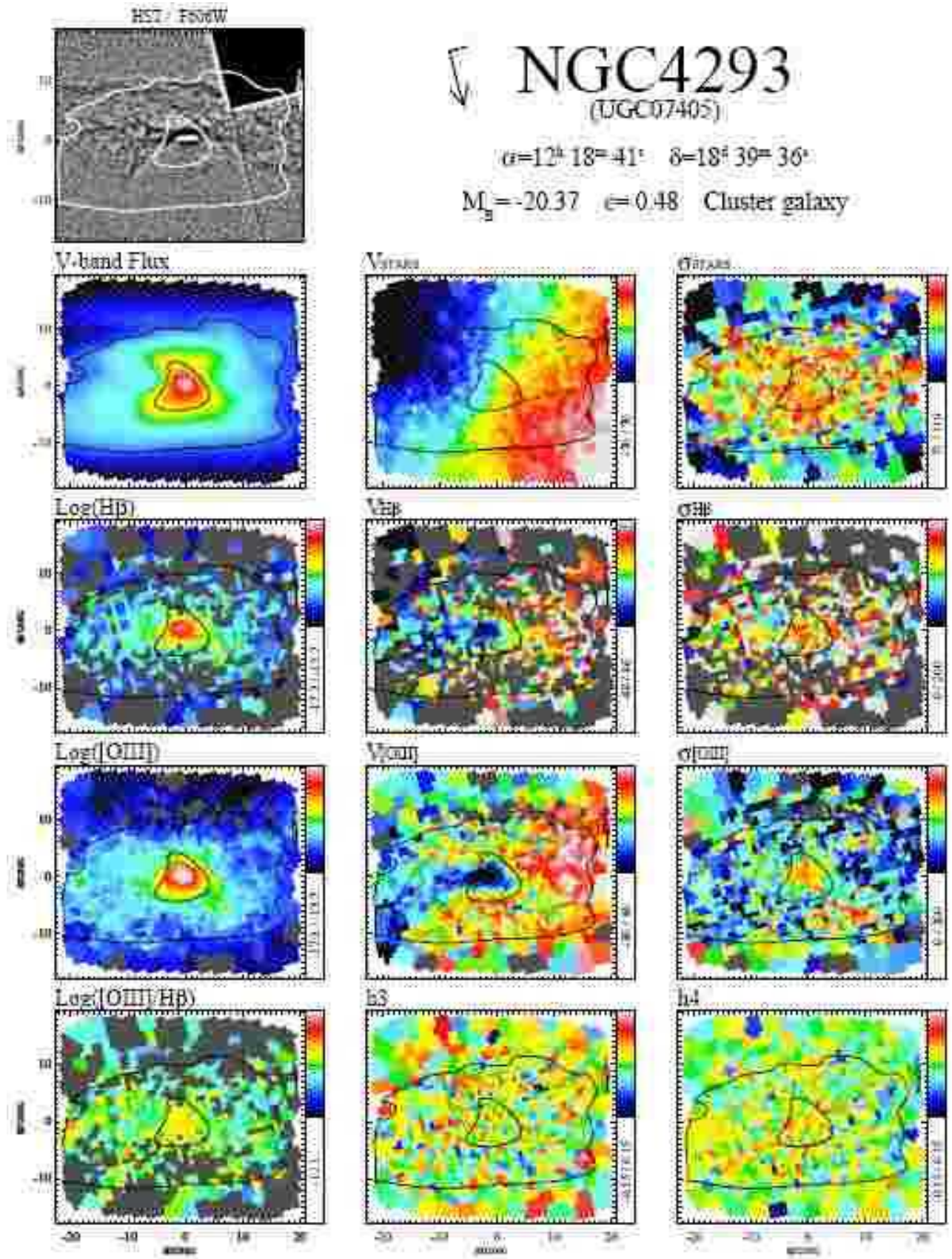


Figure 6i.

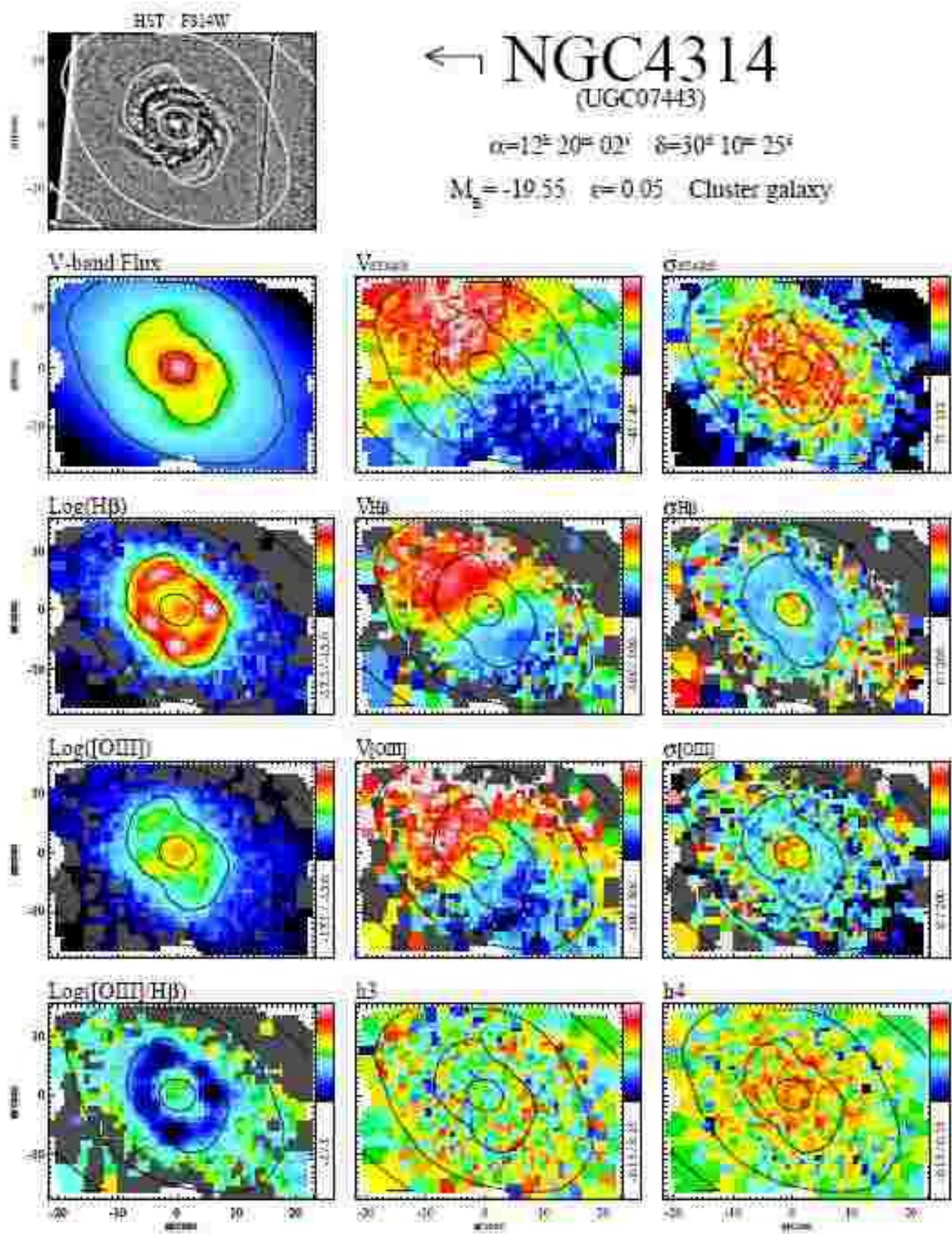


Figure 6j.

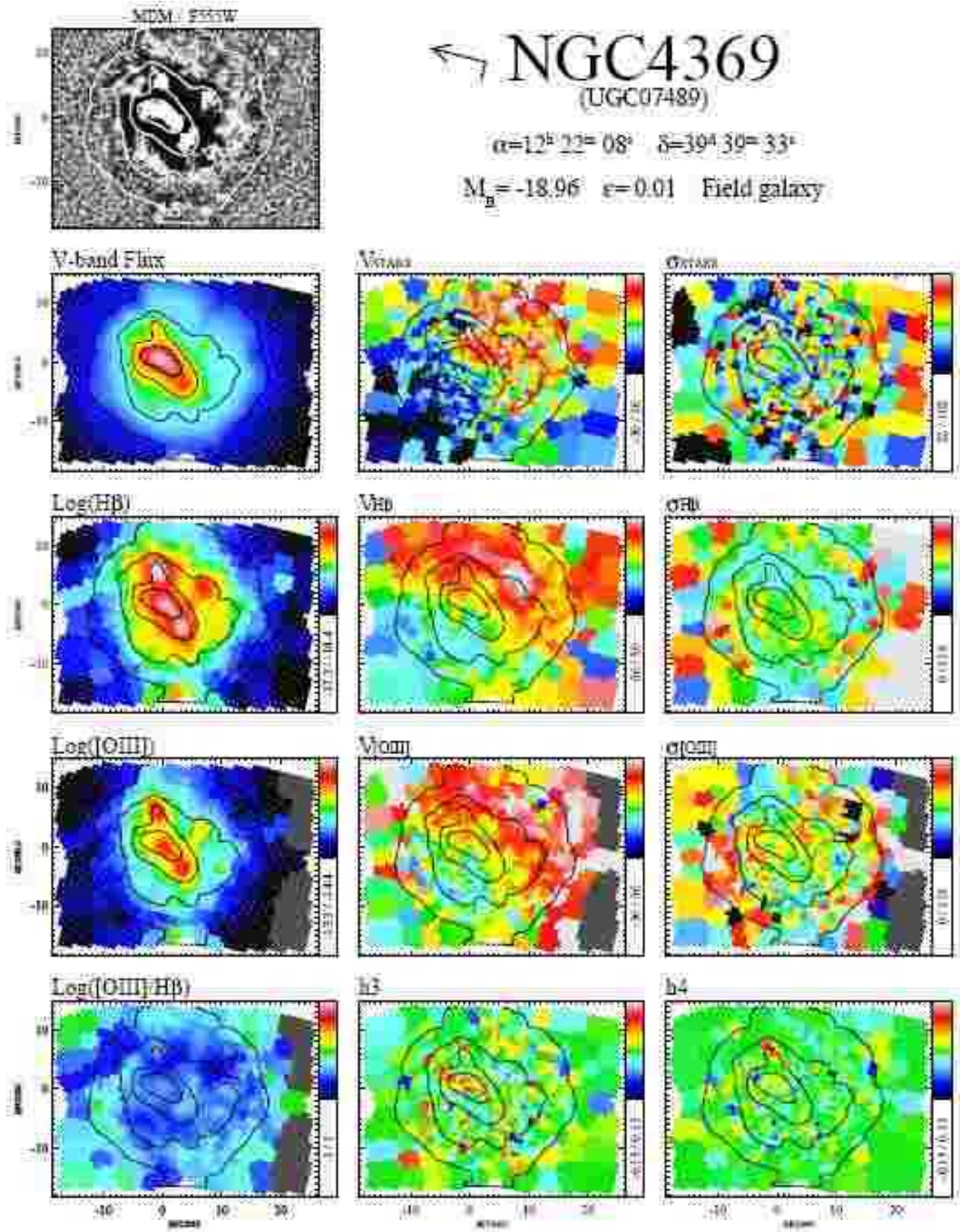


Figure 6k.

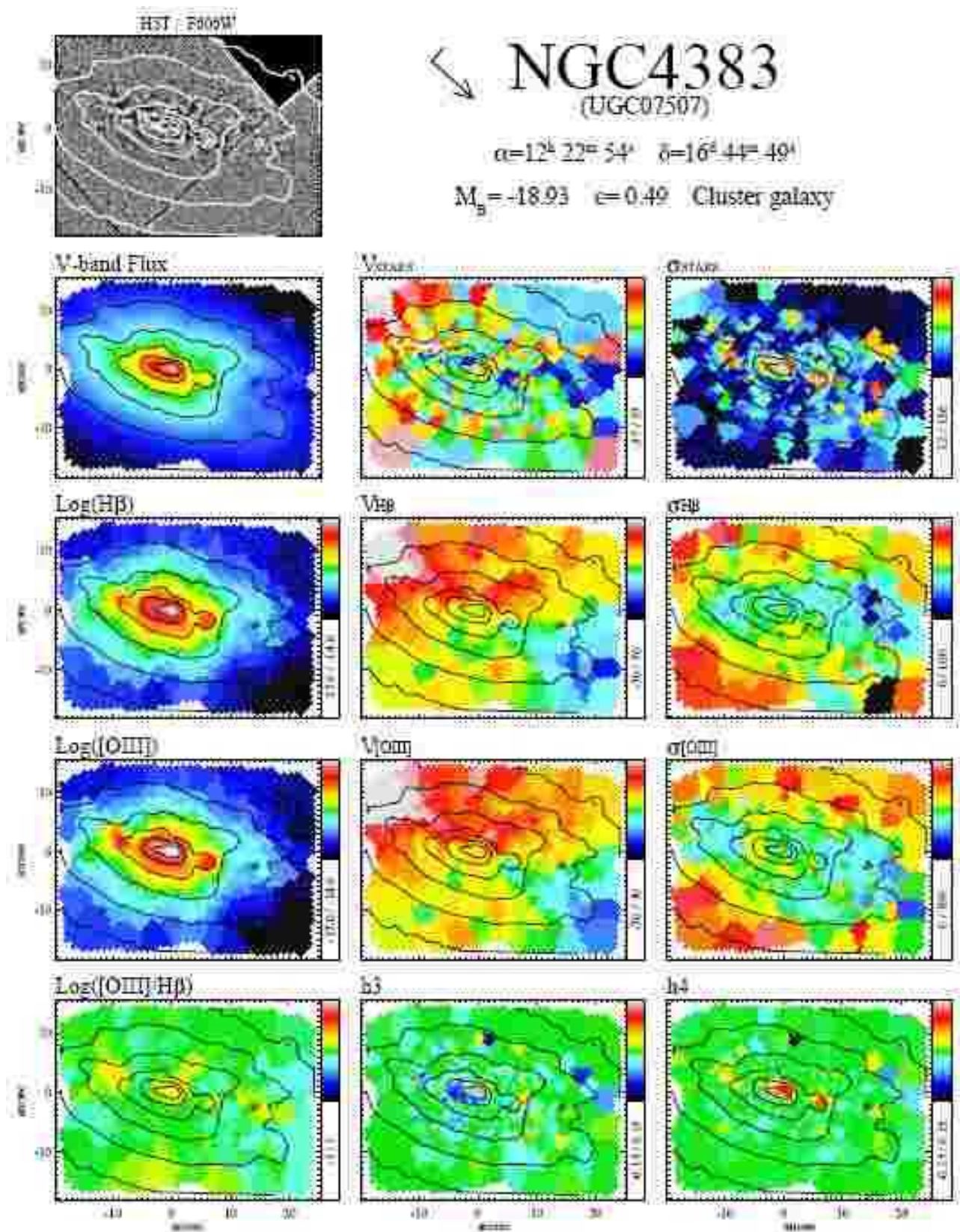


Figure 61.

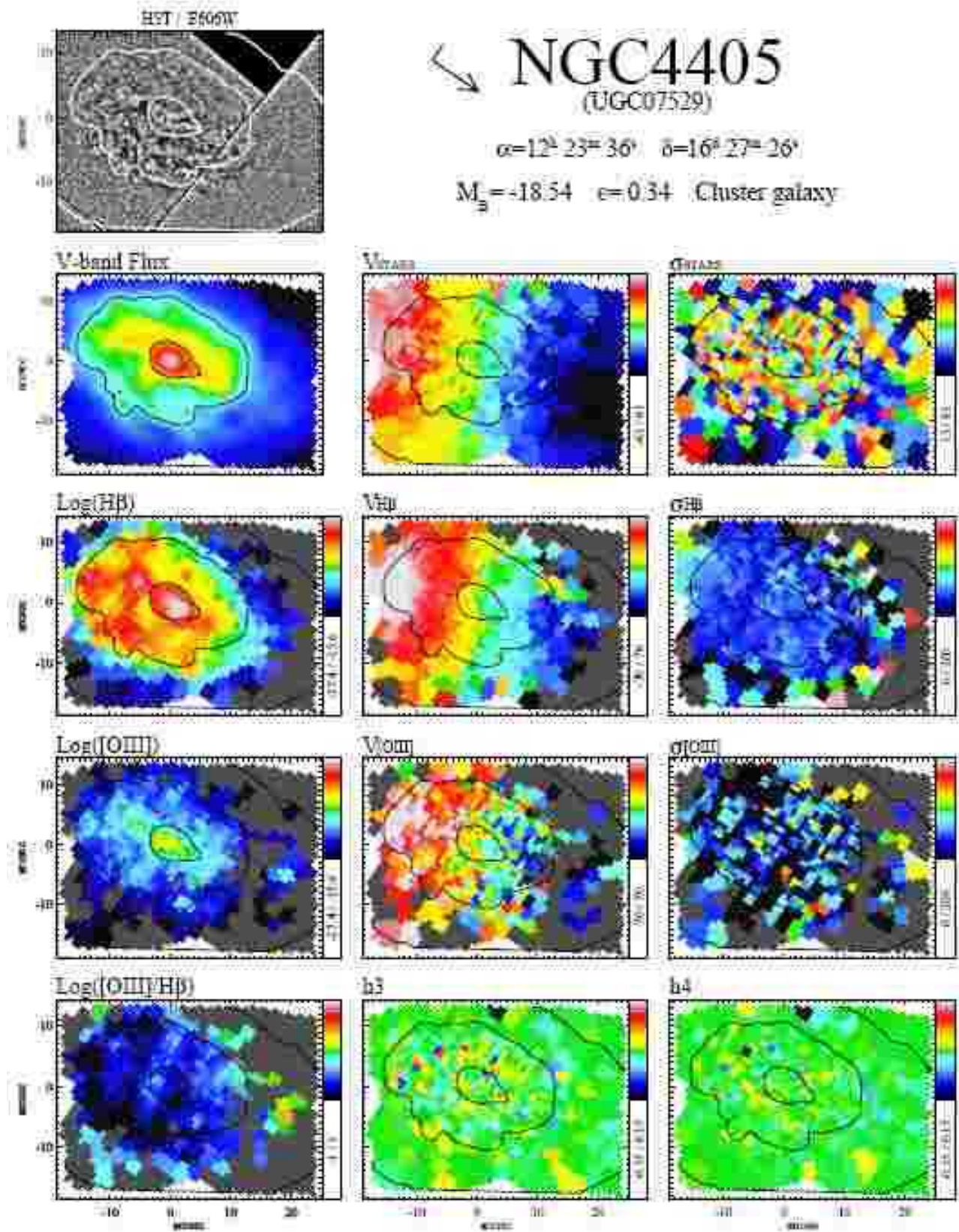


Figure 6m.

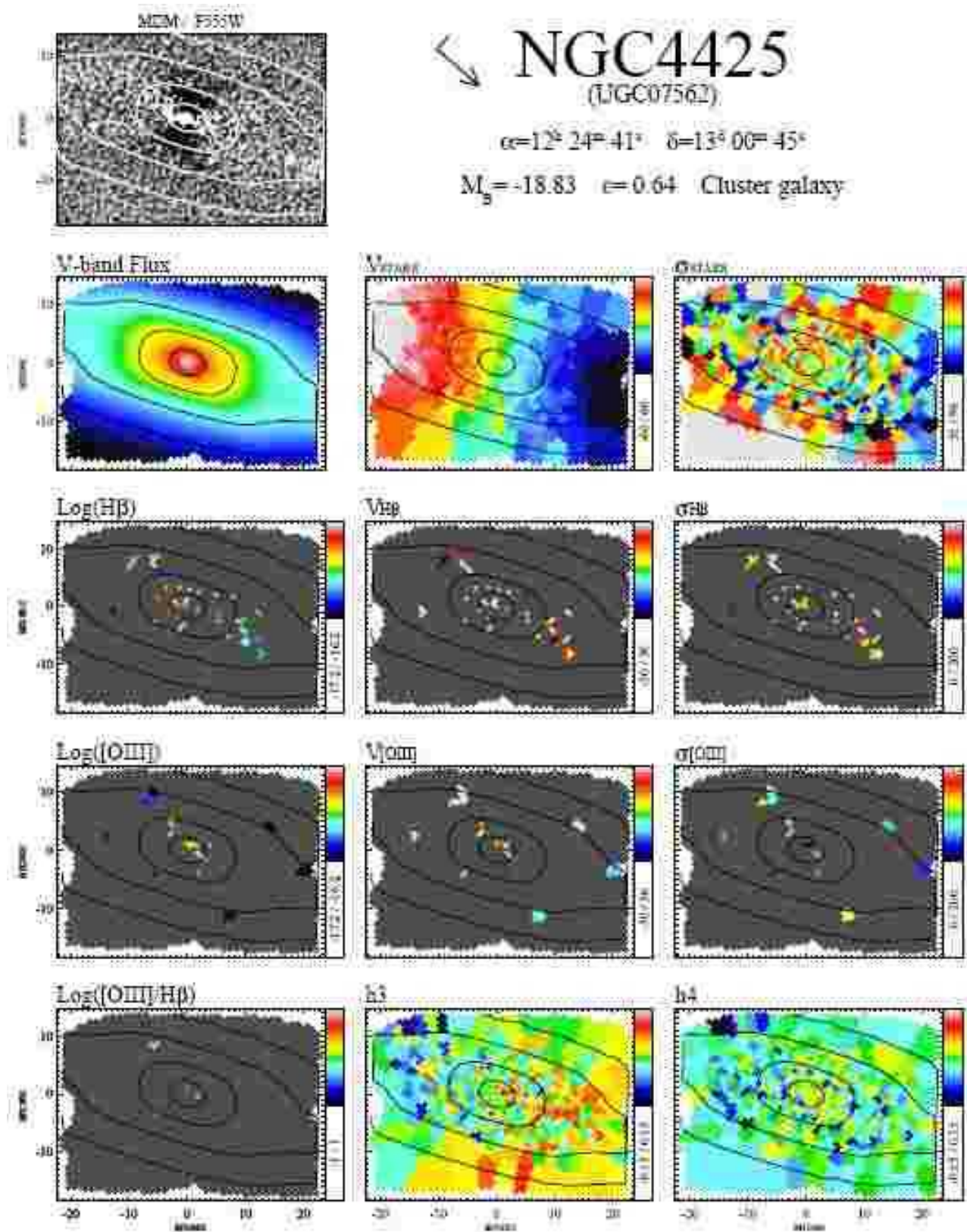


Figure 6n.

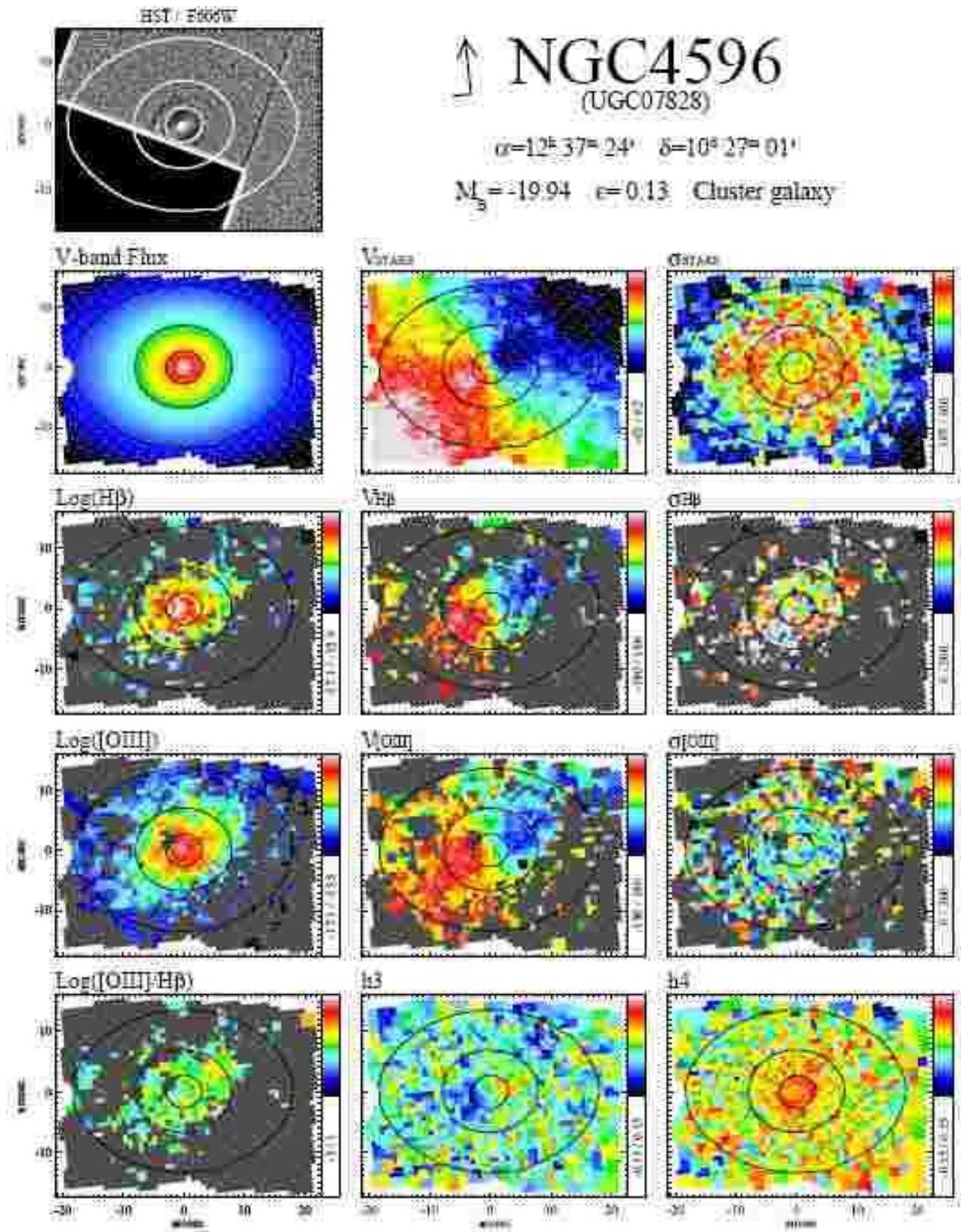


Figure 60.

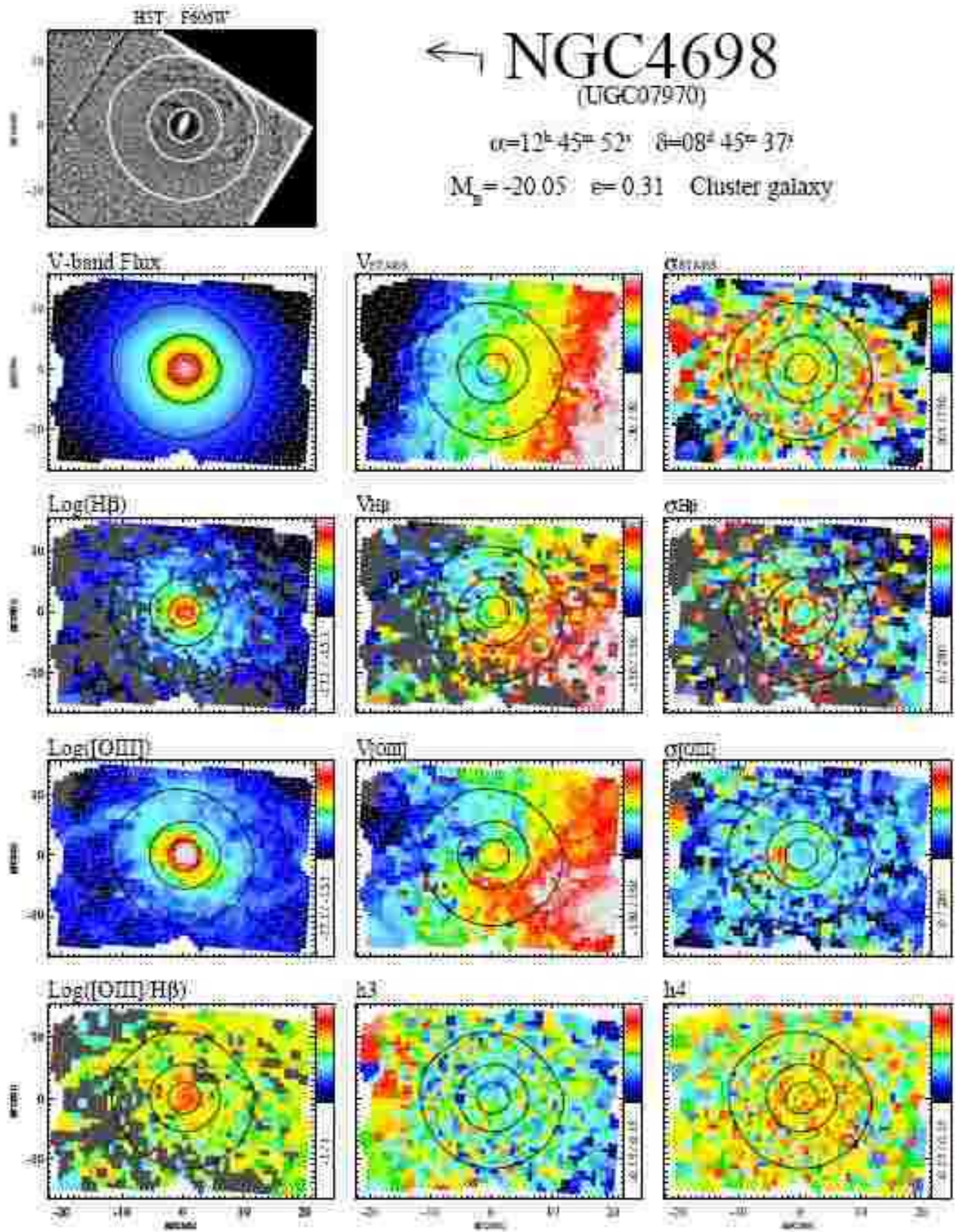


Figure 6p.

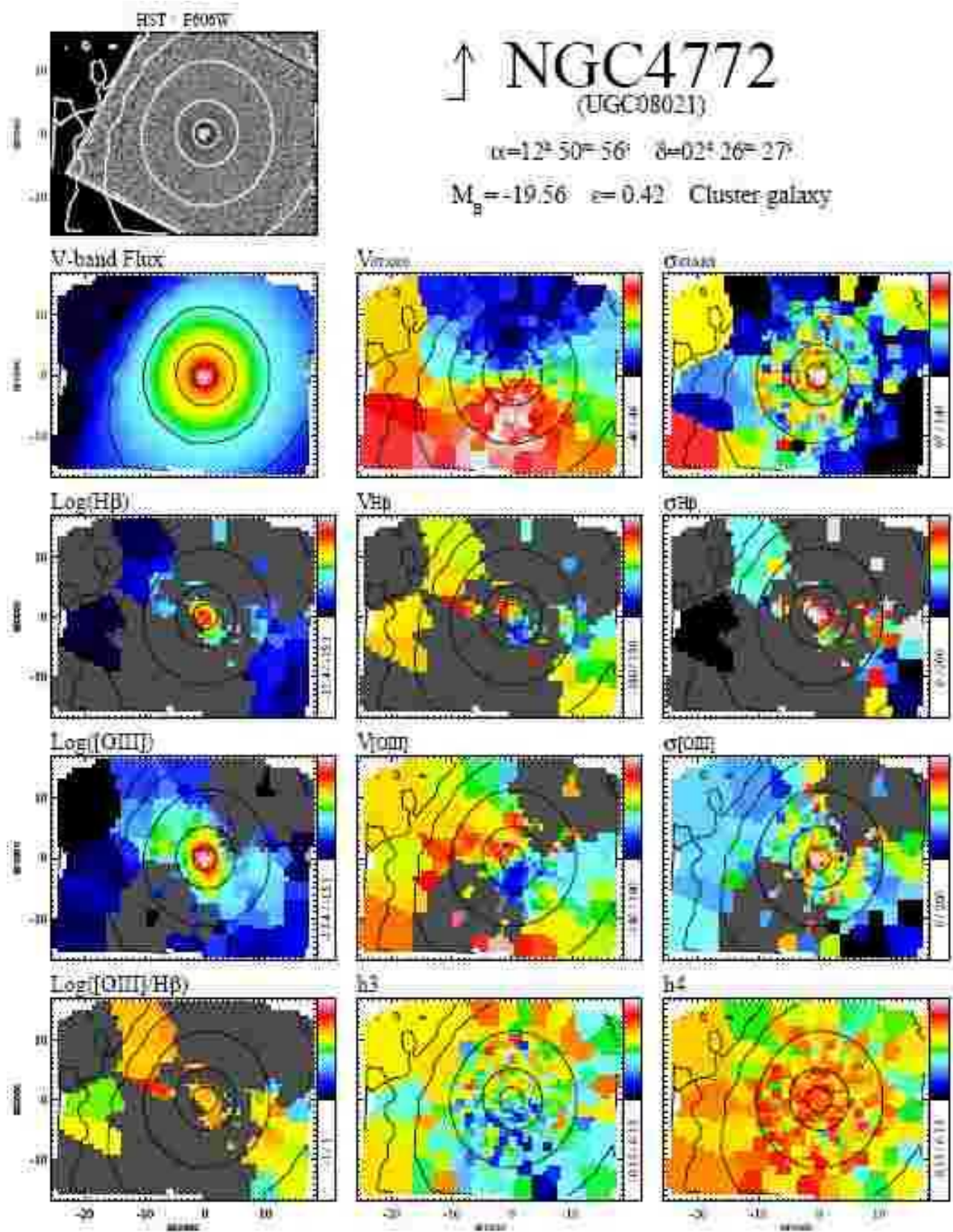


Figure 6q.

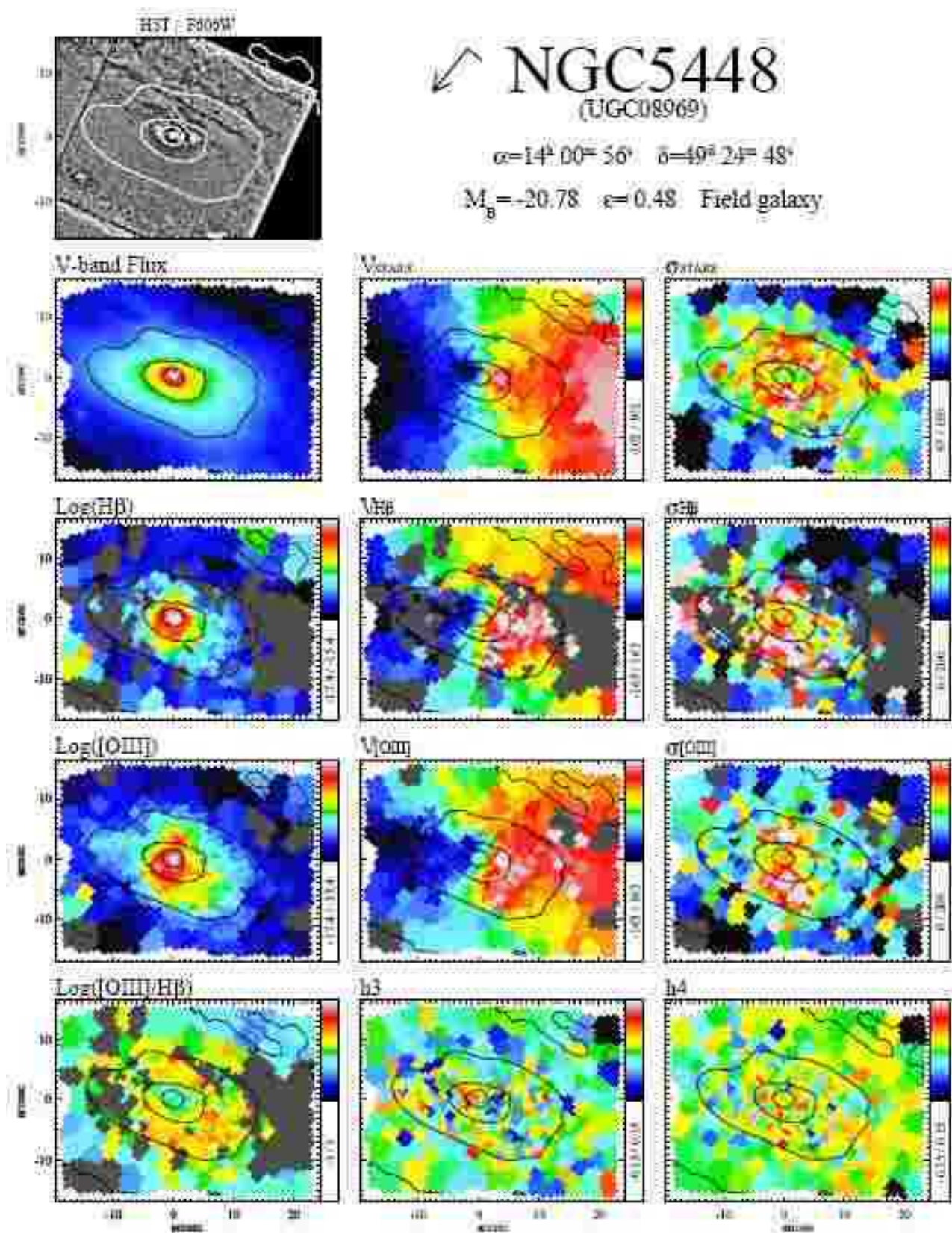


Figure 6r.

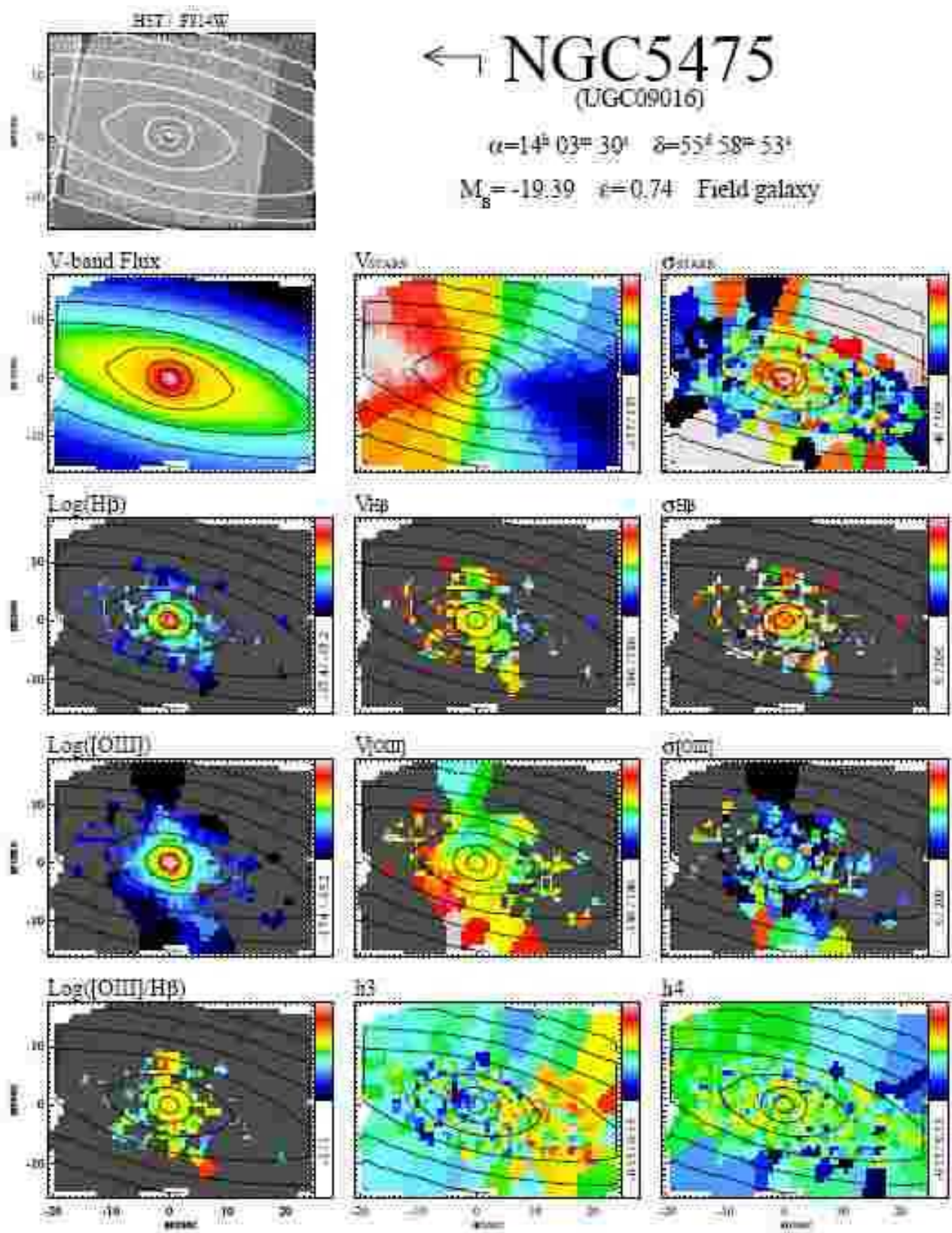


Figure 6s.

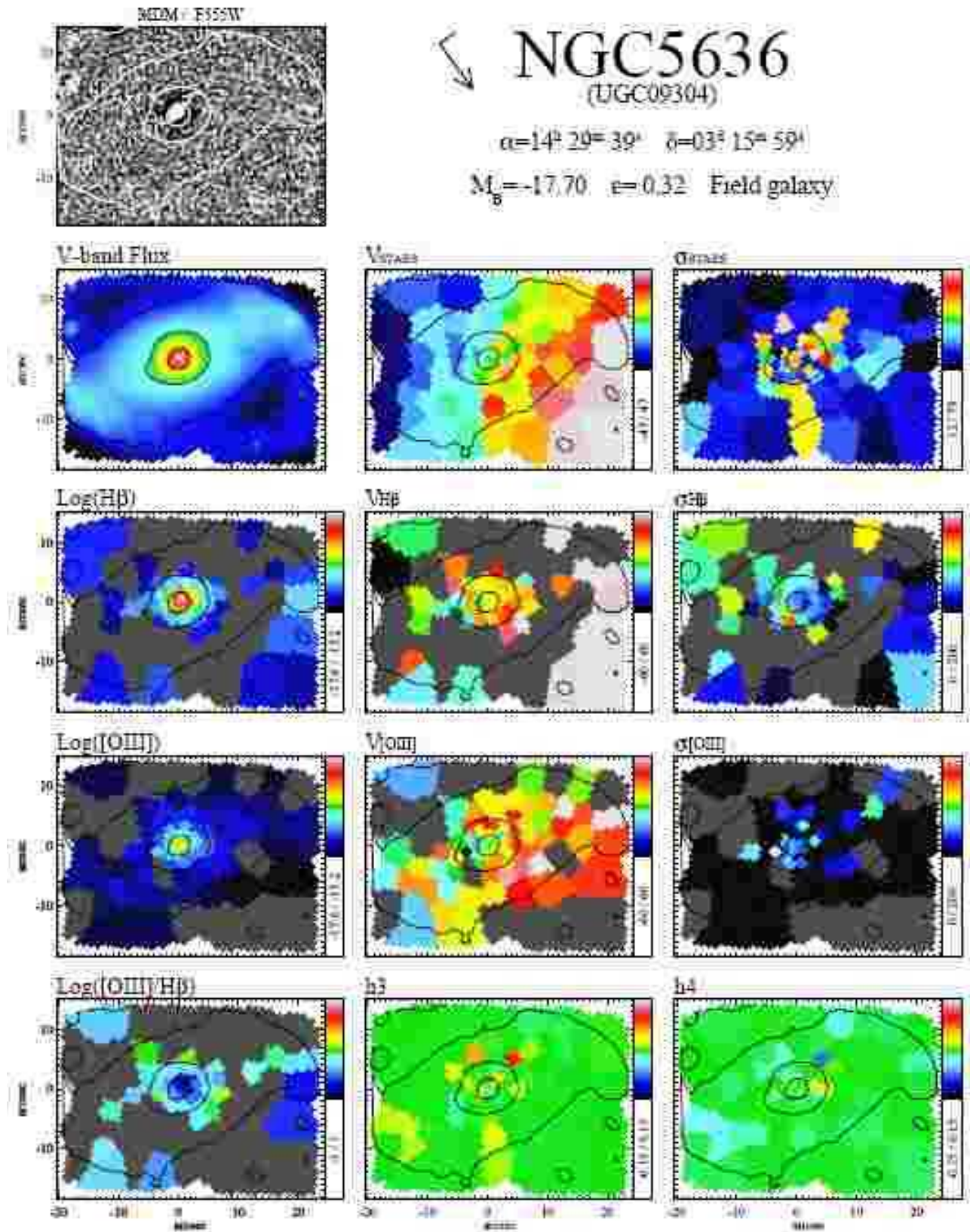


Figure 6t.

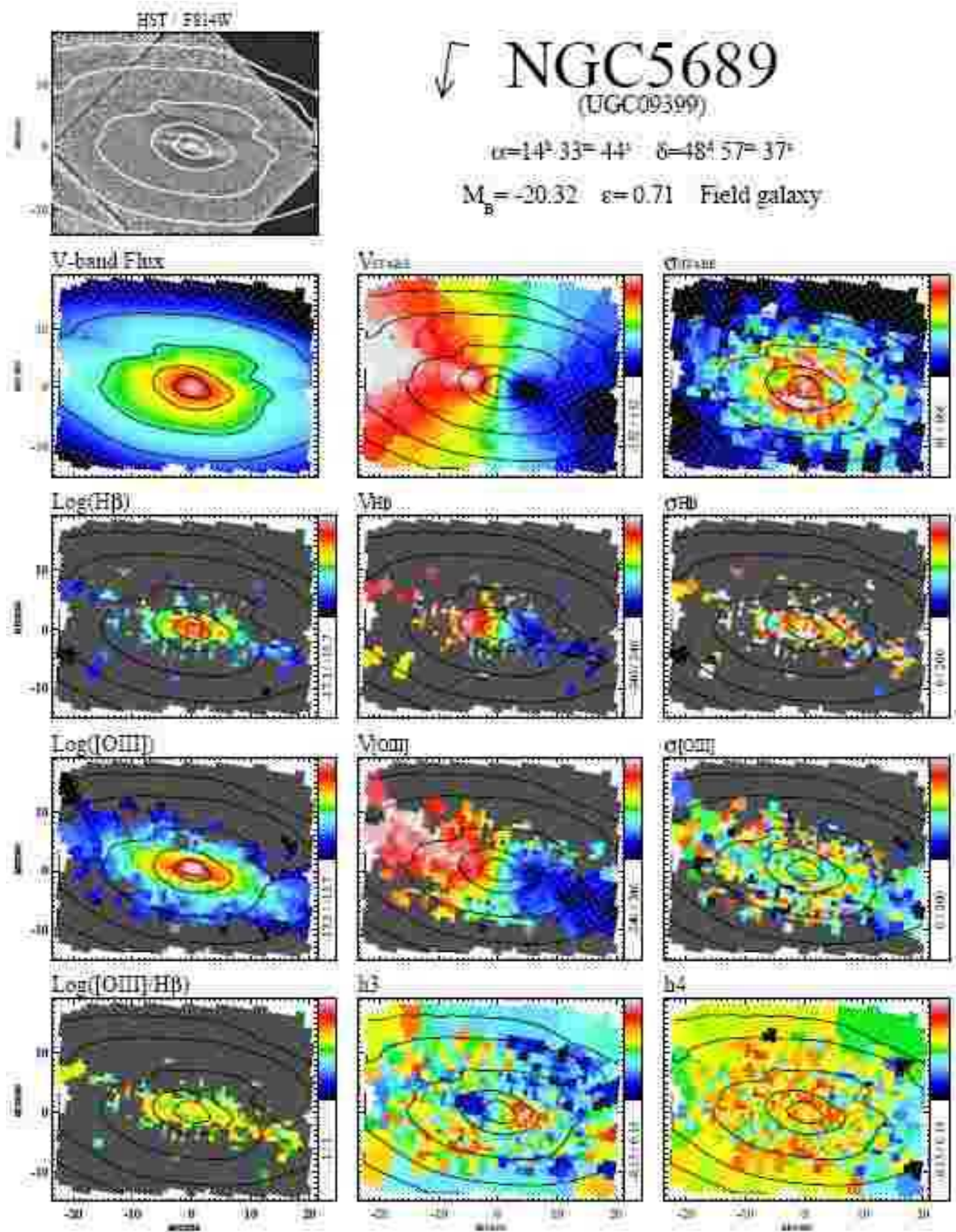


Figure 6u.

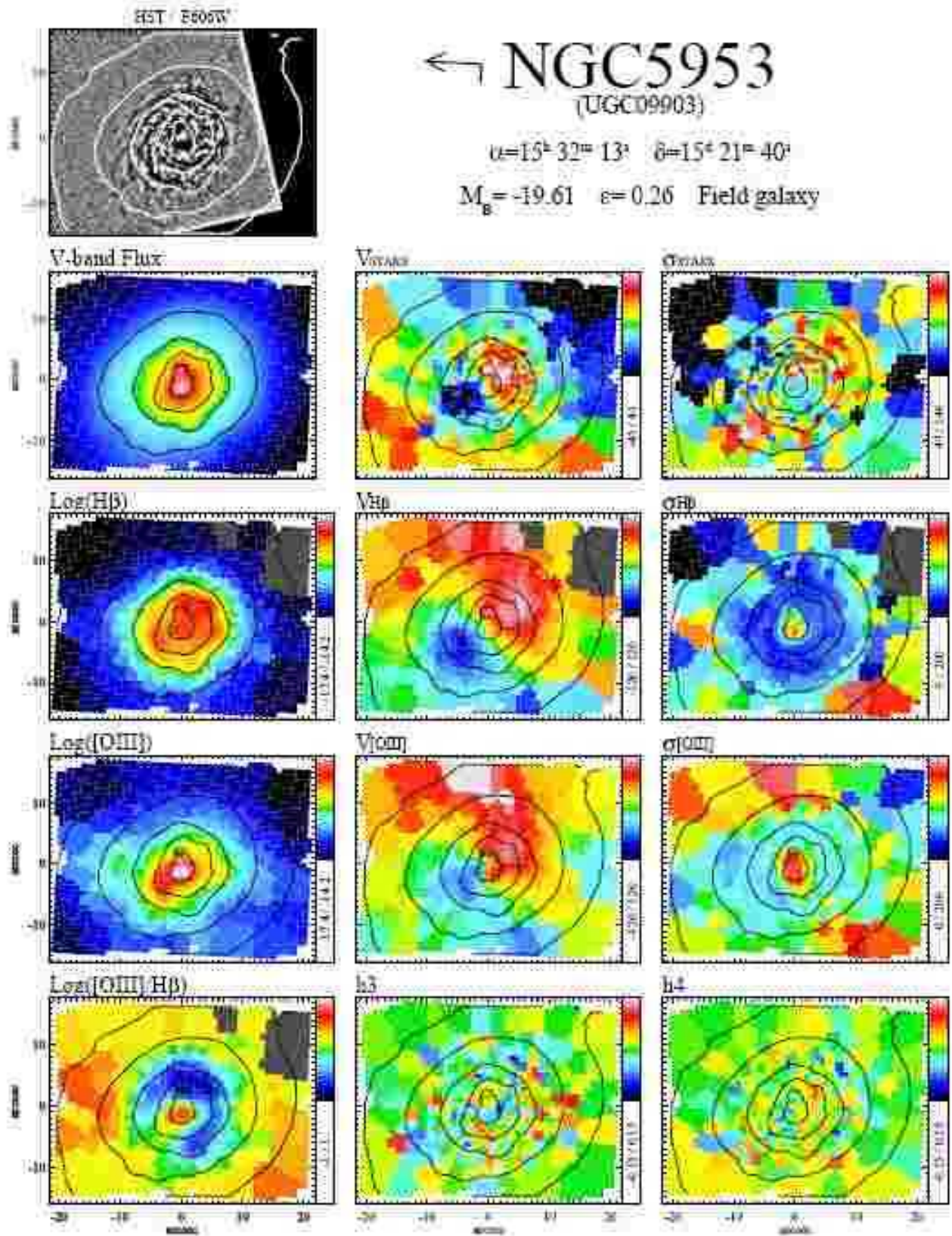


Figure 6v.

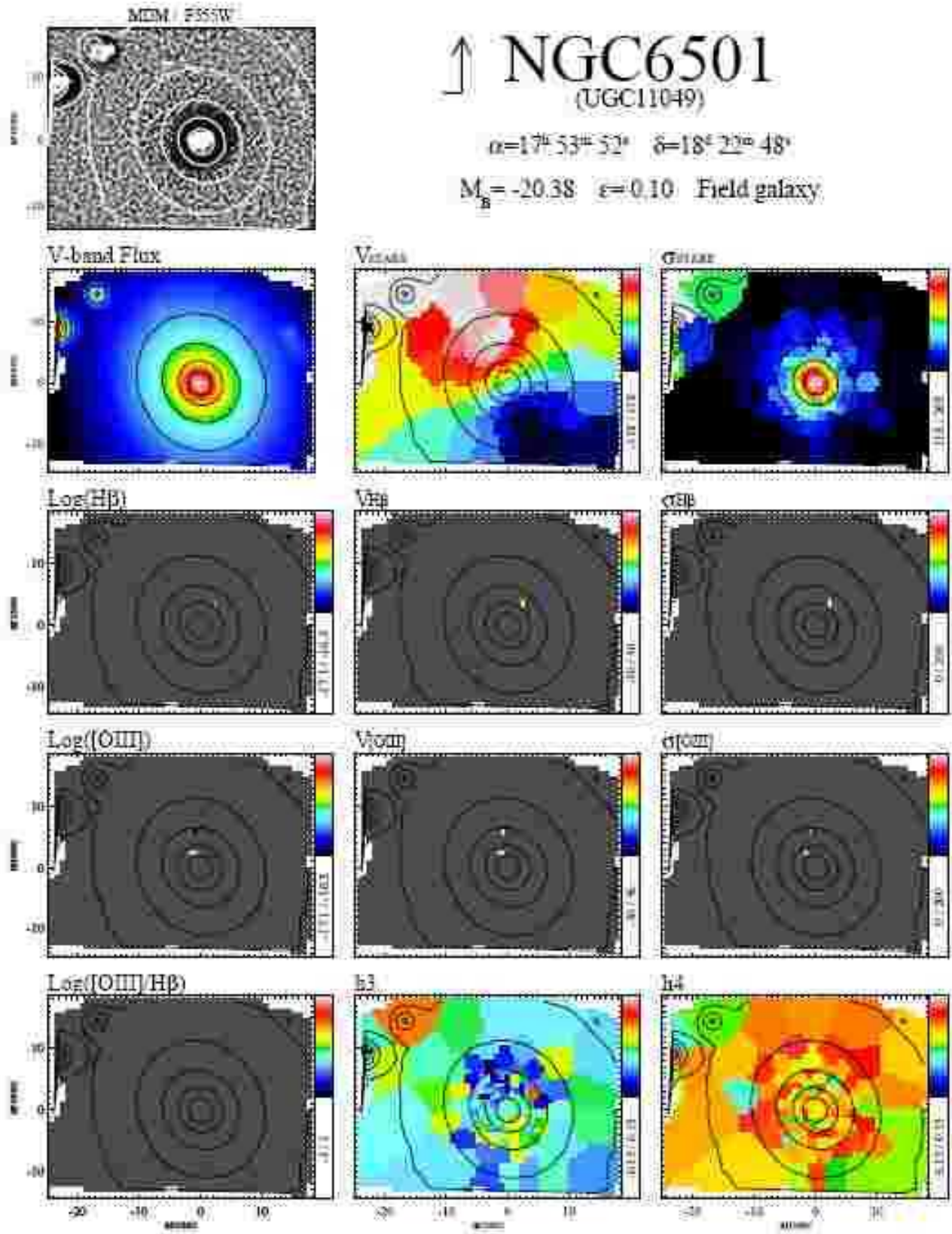


Figure 6w.

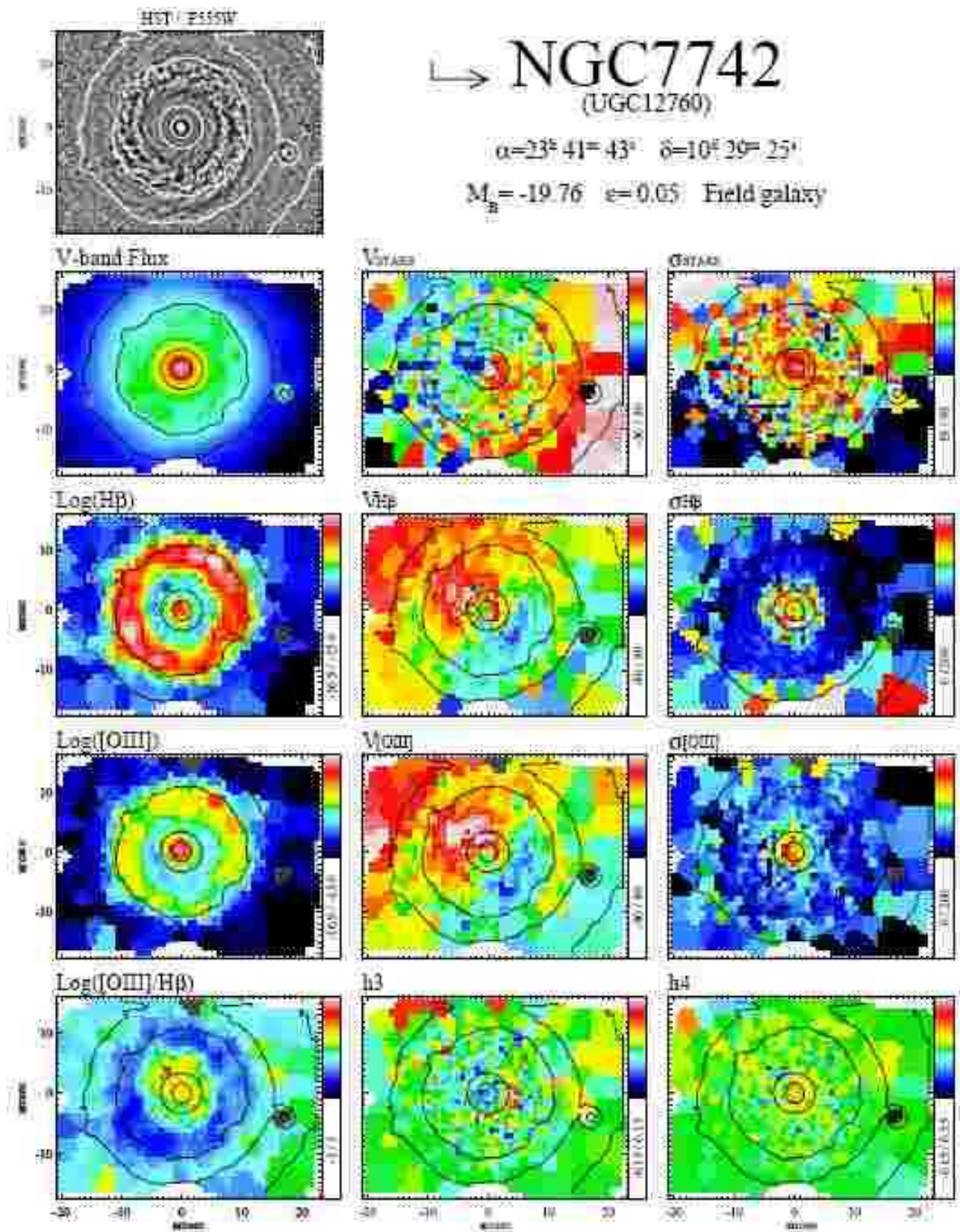


Figure 6x.

APPENDIX A: DESCRIPTION OF INDIVIDUAL GALAXIES

Here, we briefly comment on the structures observed and provide some relevant references in the literature for each galaxy.

NGC 1056 displays a complex stellar velocity field, due to the presence of significant amounts of dust. The inner parts, however, might reveal the presence of an inner disk. Unlike other cases in the SAURON survey, this feature is not accompanied by an anti-correlation with the h_3 parameter. The velocity dispersion is also patchy, although a central dip can be recognised. These properties contrast with a smooth and regular ionised-gas distribution and kinematics. The [O III]/H β ratio is low (≤ 1) all across the main disc of the galaxy. This is in agreement with previous work in the literature that had classified NGC 1056 as a H II galaxy (Veilleux et al. 1995).

NGC 2273 is a well-studied double barred galaxy (Ferruit et al. 2000). As expected in a low-inclined barred system, the SAURON stellar velocity field is misaligned with respect to the bar major axis. The zero-velocity curve displays a twist in the central $\approx 3''$. This velocity feature is also accompanied by a central dip in the velocity dispersion maps and anti-correlates with the central h_3 values, suggesting the presence of a nuclear stellar disc. The [O III] and H β ionised-gas maps show very similar distributions and kinematics. The [O III]/H β ratio is enhanced in the centre of the galaxy, in agreement with the Seyfert 2 classification of its nuclear emission (Ho et al. 1997a). Towards the end of the main bar, however, the ratio is lower, which is consistent with the presence of H II regions (Gonzalez Delgado et al. 1997).

NGC 2844 is the brightest member of a group of galaxies including also NGC 2852 and NGC 2853 (Giuricin et al. 2000). The stellar kinematics display regular velocity and velocity dispersion fields. The H β and [O III] flux maps reveal a ring-like structure, consistent with a dust ring seen in the unsharp-masking. The [O III]/H β ratio and the gas velocity dispersion are low along the ring, which is indicative of ongoing star formation. The galaxy is classified as an H II galaxy in NED. The H β and [O III] velocity fields are both regular and similar to the stellar velocity map.

NGC 3623 is a barred Sa galaxy and a member of the Leo Triplet. While there are strong indications that the two other members of the triplet (NGC 3627 and NGC 3628) are interacting, NGC 3623 appears undisturbed (Chromey et al. 1998). This galaxy contains a prominent dust lane at $\approx 15''$ East of the nucleus. The stellar velocity map is twisted with respect to the reconstructed intensity image. The h_3 parameter correlates, in the outer parts, with the stellar velocity field, giving kinematic confirmation of the presence of a large-scale bar (Bureau & Athanassoula 2005). A central disc is also present in the inner parts of the galaxy (see also Afanasiev & Sil'chenko 2005). Kinematic signatures of this disc can be seen in the stellar velocity map, in the drop of velocity dispersion, and in the anti-correlation of the h_3 parameter in the inner parts. The ionised gas shows a patchy morphology with a highly twisted zero-velocity curve and some indication of the presence of spiral arms. An H α image of the galaxy is shown in Hameed & Devereux (2005).

NGC 4220 is an almost edge-on galaxy ($i \approx 85^\circ$) that forms a non-interacting pair with NGC 4218 at $15'$ (Giuricin et al. 2000). Our unsharp-masked image displays a prominent dust lane at a distance of $5''$ north-east of the centre, which is probably part of a more extended dust ring. The presence of the dust lane is also evident in the [O III]/H β map, where the ratio is very low at that location. The SAURON reconstructed intensity image reveals a clear

boxy bulge component (Lütticke et al. 2000). The stellar velocity field exhibits cylindrical rotation. Both the [O III] and H β morphology are very similar in the central parts, but whereas the [O III] flux steadily decreases further out from the center, the H β emission remains strong also outside the centre, in particular towards East. The ionised-gas velocity fields are consistent with that of the stars.

NGC 4235 is a nearly edge-on Seyfert 1 galaxy (Jiménez-Benito et al. 2000) in a non-interacting pair with NGC 4246 at $12'$. The stellar velocity field displays regular rotation and evidence for the presence of a smaller stellar disk in the inner parts. This is supported by a decrease in velocity dispersion and h_3 anti-correlation in the centre of the galaxy. The [O III] emission is much more extended along the main disc of the galaxy than the H β emission, which is mainly confined near the centre of the galaxy. The [O III]/H β ratio is high in the centre, consistent with its classification as a Seyfert galaxy. The ionised-gas velocity maps of both H β and [O III], although patchy, are consistent with the stellar velocity field. Near-infrared surface photometry of this galaxy is presented in Peletier et al. (1999). Long-slit kinematics can be found in Corsini et al. (2003).

NGC 4245 is a barred galaxy with a prominent dust ring in the centre (Erwin & Sparke 2003). The stellar velocity field is misaligned with respect to the bar major axis. There is also evidence, in the stellar kinematics (V , σ , h_3), for a central disc in the inner $5''$. A circumnuclear ring is particularly evident in the H β flux map. The correspondingly low values of the H β velocity dispersion and [O III]/H β ratio suggests that star formation is taking place at the same location.

NGC 4274 is a double barred galaxy (Shaw et al. 1995; Erwin 2004) with significant amounts of dust in the inner parts. Despite the dust, the stellar kinematics maps show regular rotation on the main disc component of the galaxy, and also the presence of an inner fast rotating ring (detected in the V and σ maps). As in NGC 4245, the signatures of the star-forming ring are easily identifiable in the ionised-gas maps. An H α image is presented in Hameed & Devereux (2005).

NGC 4293 is a relatively highly-inclined galaxy with a large-scale bar (Laurikainen & Salo 2002). The unsharp-masked image displays a strong dust lane passing through the nucleus and another dust lane about $7''$ south of the centre. No correspondence between the dust lanes and features in the ionised-gas maps is found. We find no signs of ongoing star formation in the [O III]/H β map, in agreement with Koopmann & Kenney (2004). The stellar kinematics is regular with no signs of inner kinematic components.

NGC 4314 is a low-inclined, well studied barred galaxy in the Virgo cluster (Benedict et al. 1996; Pérez-Ramírez et al. 2000), mainly known for a nuclear star-forming ring in the inner $10''$. The stellar kinematics displays regular rotation around the minor axis of the galaxy. The kinematics of the ionised gas is consistent with that of the stars. The presence of the nuclear ring is clearly visible in the H β flux and velocity dispersion maps. The [O III] distribution, however, is more concentrated in the centre of the galaxy. The different morphology of the two emission lines enhances the signature of the star-forming ring in the [O III]/H β map.

NGC 4369 is a low-inclined galaxy that shows a small rotational velocity amplitude in our stellar velocity field. The stellar kinematics is significantly affected by dust, as seen from the patchiness of the velocity dispersion map. The ionised-gas flux maps show evidence for two star-forming regions at both sides of the galactic centre (Usui et al. 1998). The [O III]/H β map displays overall very low values overall. Near-infrared surface photometry of this galaxy

is presented in Peletier et al. (1999), and $H\alpha$ imaging can be found in Hameed & Devereux (2005).

NGC 4383 is a starburst galaxy in the Virgo cluster (Rubin et al. 1999). The stellar kinematics show a complex picture with no clear sense of rotation in the inner parts, possibly due to the presence of significant amounts of dust. The SAURON ionised-gas maps are also difficult to interpret, although they are consistent with $H\alpha$ observations by Koopmann & Kenney (2004), which reveal a bi-conical filamentary structure suggestive of a starburst outflow. The galaxy also displays enhanced star formation (Koopmann & Kenney 2004).

NGC 4405 is a Sa galaxy with no prominent spiral structure, but with evidence of central dust lanes. The stellar velocity map is regular. Although there is a drop in velocity dispersion at the centre of the galaxy, no evidence for an inner component is found in either the stellar velocity or h_3 maps. The $H\beta$ gas map displays several *clumps* around the centre, as opposed to the [O III] map where the distribution is smoother. Both the $H\beta$ and [O III] velocity maps show regular rotation, consistent with that of the stars. Ongoing star formation is confined in the central dust disc seen in the unsharp-masked image (Koopmann & Kenney 2004).

NGC 4425 is a highly inclined galaxy without much dust. The SAURON reconstructed intensity image reveals a boxy bulge component (Lütticke et al. 2000). The stellar velocity field exhibits cylindrical rotation. The stellar velocity dispersion is generally low ($\leq 100 \text{ km s}^{-1}$). The ionised-gas maps show only patchy traces of emission.

NGC 4596 is a non-interacting strongly barred galaxy (Gerssen et al. 1999). The SAURON stellar velocity field displays regular rotation along an axis misaligned with respect to the photometric major axis. There is evidence for a disc-like component in the inner $5''$ region, that it is also apparent in the velocity dispersion and h_3 maps. The distribution and kinematics of both $H\beta$ and [O III] are aligned with the stellar kinematic major axis. Gerssen et al. (1999), using the Tremaine-Weinberg method, reported that NGC 4596 has a fast bar.

NGC 4698 is a low-luminosity Seyfert 2 galaxy (Ho et al. 1995) that is thought to have experienced a major or intermediate-mass merger (Bertola et al. 1999, but see also Sarzi et al. 2000). The SAURON stellar velocity field displays regular rotation around the minor axis. The inner parts however (i.e. $5''$) appear to be rotating perpendicularly to the main body of the galaxy, consistent with a nuclear disc in our unsharp-masked image (see also Pizzella et al. 2002). We note, however, that no clear evidence for such decoupled inner component is found in either the velocity dispersion or h_3 maps. This result is consistent with long-slit results from Bertola et al. (1999). The ionised-gas distribution is rather regular, with $H\beta$ being more extended than [O III]. The velocity fields of the ionised-gas are consistent with that of the stars. Koopmann & Kenney (2004), from $H\alpha$ observations, reported a low of level star formation across the disc.

NGC 4772 is a galaxy located at the boundaries of the Virgo cluster (Haynes et al. 2000). A strong dust lane is seen to the East. The stellar kinematics display regular rotation along the major axis of the galaxy. The unsharp-masked image reveals a small dusty disc in the centre of the galaxy, the orientation of which seems consistent with that of the ionised gas in the central $5''$. In these regions both the $H\beta$ and [O III] lines suggest ordered rotation for the gas, almost in the opposite sense of the stars, in agreement with Haynes et al. (2000). The ionised-gas emission also extends beyond the central regions, in particular for the [O III] emission. The observed morphology is consistent with the narrow-band

observations of Haynes et al. (2000), suggesting that the gas emission observed at the north-eastern and south-western corner of the SAURON field comes from an outer ring of gas on the main galactic-disk plane. The [O III] kinematics is more complex at larger radii, but suggests a warping of the direction of maximum rotation towards the galaxy major axis.

NGC 5448 is an active barred galaxy (Ho et al. 1997a; Eskridge et al. 2002). The stellar kinematics display a regular disc, and signatures of an inner fast rotating component in the central $\approx 5''$. The $H\beta$ distribution is more concentrated than the [O III]. The ionised-gas kinematics features an 'S-shaped' zero-velocity curve, suggestive of gas radial motions. The [O III]/ $H\beta$ map shows a drop in the centre of the galaxy, with the same extent and location of the inner component seen in the stellar kinematics and dust disc in the unsharp-masked image. We refer the reader to Fathi et al. (2005) for a detailed study of this galaxy using SAURON.

NGC 5475 is an isolated, nearly edge-on galaxy (Balcells & Peletier 1994). The SAURON stellar kinematics exhibits a fast rotating stellar disc aligned with the photometric major axis of the galaxy (see also Falcón-Barroso et al. 2003). The [O III] emission, however, extends further out and along the galaxy minor axis. Although disturbed, the ionised-gas kinematics further suggests evidence for polar rotation along the major axis of the galaxy.

NGC 5636 is a strongly barred galaxy in a non-interacting pair with NGC 5638 at $2'$. This galaxy is the smallest and has the lowest apparent magnitude of our sample ($m_B = 13.7$, from RC3). The direction of the maximum stellar rotation is misaligned with respect to the bar major axis. The stellar velocity dispersion is one of the lowest in the sample. In a large fraction of the SAURON map the values represent an upper limit. The ionised-gas is concentrated around the centre of the galaxy, where very low values of the [O III]/ $H\beta$ ratio suggest ongoing star formation.

NGC 5689 is an almost edge-on barred galaxy with a box-shaped bulge (Lütticke et al. 2000). It is the brightest non-interacting member of a group formed by NGC 5682, NGC 5683, and NGC 5693 (Giuricin et al. 2000). The unsharp-masked image displays a dust lane $\approx 5''$ south of the nucleus. The stellar kinematics shows prominent signatures of an inner, fast-rotating disc component (i.e. central increase in rotational velocity, velocity dispersion drop, and $h_3 - V$ anti-correlation). See also Falcón-Barroso et al. (2003). The ionised-gas shows an elongated disc-like distribution and fast rotation.

NGC 5953 is a Seyfert 2 galaxy closely interacting with NGC 5954 (Reshetnikov 1993; Gonzalez Delgado & Perez 1996). The SAURON stellar kinematics displays large-scale rotation and a kinematically decoupled component in the central $10''$. The [O III] ionised gas presents an elongated distribution towards NGC 5954 (i.e. NE of NGC 5953 centre), which is associated with radio emission (Jenkins 1984), whereas the $H\beta$ distribution is symmetric around the galactic centre and it is consistent with a dust ring seen in the unsharp-masked image. The ionised-gas kinematics of the central component follows that of the stars in the inner parts, and it is in good agreement with that of Hernández-Toledo et al. (2003) from Fabry-Perot observations of the [N II] emission-line. The [O III]/ $H\beta$ ratio map exhibits very low values in the location of the circumnuclear region and it is enhanced in the very centre of the galaxy. Our results are similar to those measured by Yoshida et al. (1993) in the inner region (i.e. [O III]/ $H\beta=0.14-0.41$), and are consistent with a star-forming ring surrounding an active galactic nucleus. The combined observations presented here suggests that we might be witnessing the early stages in the formation of a kine-

matically decoupled component. Further analysis including stellar populations is, however, necessary to confirm this hypothesis.

NGC 6501 is galaxy that is part of a group formed by NGC 6467, NGC 6495, PGC 61102 and NGC 6500 (Giuricin et al. 2000). The SAURON stellar velocity field displays regular rotation along the major axis of the galaxy. The stellar velocity dispersion map shows the highest value in our sample ($\approx 270 \text{ km s}^{-1}$) and a steep gradient decreasing towards the outer parts. No ionised-gas was detected in this galaxy, in agreement with earlier work (Cid Fernandes et al. 2004).

NGC 7742 is a well-known face-on Seyfert galaxy hosting a prominent star-forming ring surrounding a bright nucleus (see Paper II). Despite the low inclination, the stellar kinematics show overall rotation at large-scale, but also in the inner parts. The ring structure is evident in both the $\text{H}\beta$ and $[\text{O III}]$ distribution and velocity dispersions. The $[\text{O III}]/\text{H}\beta$ map displays very low values at the location of the ring, also visible in the unsharp-marked image, suggestive of current star formation. The ionised-gas counter-rotates with respect to the stars.